

Uncovering diffusive states of the yeast proton pump, Pma1, and how labeling method can change diffusive behavior

Mary Lou P. Bailey,^{1,2} Susan E. Pratt,^{1,3} Yongdeng Zhang,⁴ Michael Hinrichsen,⁵
Joerg Bewersdorf,^{1,3,4,6} Lynne J. Regan,⁷ and Simon G. J. Mochrie^{1,2,3,*}

¹*Integrated Graduate Program in Physical and Engineering Biology,
Yale University, New Haven, Connecticut 06520, USA*

²*Department of Applied Physics, Yale University, New Haven, Connecticut 06520, USA*

³*Department of Physics, Yale University, New Haven, Connecticut 06520, USA*

⁴*Department of Cell Biology, Yale School of Medicine, New Haven, CT 06520, USA*

⁵*Department of Molecular Biophysics and Biochemistry,
Yale University, New Haven, Connecticut 06511, USA*

⁶*Department of Biomedical Engineering, Yale University, New Haven, Connecticut 06511, USA*

⁷*Institute of Quantitative Biology, Biochemistry and Biotechnology,*

Center for Synthetic and Systems Biology, School of Biological Sciences, University of Edinburgh, UK

(Dated: April 6, 2022)

We present and analyze video-microscopy-based single-particle-tracking measurements of the budding yeast (*Saccharomyces cerevisiae*) membrane protein, Pma1, fluorescently-labeled either by direct fusion to the switchable fluorescent protein, mEos3.2, or by a novel, light-touch, labeling scheme, in which a 5 amino acid tag is directly fused to the C-terminus of Pma1. This tag specifically and reversibly binds to a tetratricopeptide repeat affinity protein (TRAP) which is directly fused to mEos3.2 [ChemBioChem 17, 1652 (2016)]. The diffusivity distributions of these two populations of single particle tracks differ significantly, demonstrating that labeling method can be an important determinant of diffusive behavior. To further analyze the diffusive dynamics, we applied perturbation expectation maximization (pEMv2) [Physical Review E 94, 052412 (2016)], which sorts trajectories into the statistically-optimum number of diffusive states. For both TRAP-labeled Pma1 and Pma1-mEos3.2, pEMv2 sorts the tracks into two diffusive states: an essentially immobile state and a more mobile state. However, the mobile fraction of Pma1-mEos3.2 tracks is much smaller (~ 0.1) than the mobile fraction of TRAP-labeled Pma1 tracks (~ 0.5). In addition, the diffusivity of Pma1-mEos3.2's mobile state is several times smaller than the diffusivity of TRAP-labeled Pma1's mobile state. Thus, Pma1-mEos3.2 is essentially immobile. By contrast, 50% of TRAP-labeled Pma1 molecules are mobile with a diffusivity, typical for membrane proteins. To critically assess pEMv2's performance, we compare the diffusivity and covariance distributions of the experimental pEMv2-sorted populations to corresponding theoretical distributions, assuming that Pma1 displacements realize a Gaussian random process. The experiment-theory comparisons for both the TRAP-labeled Pma1 and Pma1-mEos3.2 reveal good agreement, bolstering the pEMv2 approach. Overall, this work develops a template for how to analyze heterogeneous biological diffusion data. It also suggests that it is necessary to consider the impact of labeling method when studying intrinsic dynamics in living cells.

I. INTRODUCTION

The goals of this paper are two-fold. The first goal is to carefully examine the extent to which the measured diffusive behavior of a protein of interest—in this case, the budding yeast (*Saccharomyces cerevisiae*) membrane protein, Pma1 [1–12]—in a heterogeneous, biological environment—in this case, the cell membrane—can be convincingly described in terms of a limited number of discrete diffusive states, each with its own diffusive properties. Such diffusive states might correspond to the protein of interest being bound to different binding partners or being located in different local environments. For Pma1, we find that the observed population of single-molecule trajectories can be well-described in terms of

just two diffusive states. One of these states corresponds to simple diffusion. The other is essentially immobile.

Our second goal is to quantify any differences between the diffusivities and displacement covariances exhibited by Pma1, labeled in two different ways. The first labeling method—which we refer to as “TRAP labeling”—is a light-touch method in which wild-type Pma1 is replaced with a version of Pma1, in which a 5 amino acid tag is directly fused to the C-terminus of Pma1 [13–17]. This is done in cells expressing a version of a fluorescent protein engineered to bind the tag, thus labeling Pma1. Second is the commonly used direct-labeling method, which replaces wild-type Pma1 with a Pma1-fluorescent protein direct-fusion. The different diffusive behavior of these two differently labeled proteins, that we observe, demonstrates that it may be necessary to broadly employ minimally-perturbing labeling schemes in order to fully realize and study intrinsic biological behavior in live cells.

* simon.mochrie@yale.edu

This paper is organized as follows. In Sec. II, we present necessary background material. Sec. II A briefly summarizes what is known about Pma1. Sec. II B describes the TRAP labeling method. In Sec. II C, we review the perturbation Expectation Maximization (pEMv2) algorithm, which determines the number of unique diffusive states within a population of single particle tracks and sorts individual tracks into those states. In Sec. II D, we review theoretical results for probability distributions of two-dimensional displacement covariance matrix elements [18], which can be compared to the corresponding experimental distributions.

In Sec. III A, we describe the yeast strains employed in this study and how samples were prepared. We describe the microscopy setup used to collect the data in Sec. III B, and the methods we used for single particle tracking in Sec. III C. In Sec. III D, we describe how we generate simulated particle tracks.

Sec. IV presents and discusses our results. In Sec. IV A, we present microscopy images of the strains studied. In contrast to cells where Pma1 is expressed as a fusion protein with the fluorescent proteins, mCherry and EGFP, which show defective growth and behavior, we find that cells expressing Pma1-mEos3.2 do not show a growth defect, nor does Pma1-mEos3.2 mislocalize to the vacuole. However, these gross observations do not rule out more subtle differences in behavior between Pma1-mEos3.2 and TRAP-labeled Pma1.

In Sec. IV B, we present the experimental track length distributions of TRAP-labeled Pma1 and Pma1-mEos3.2, and show that the lifetime of TRAP-labeled Pma1 tracks is shorter than that of Pma1-mEos3.2. We interpret this difference in lifetime in terms of a non-zero TRAP-peptide unbinding rate, which allows us to estimate this rate to be about 6 s^{-1} .

To examine the differences between the diffusive behavior of TRAP-labeled Pma1 and Pma1-mEos3.2, we subjected both of these populations of trajectories to pEMv2 analysis [19–21]. In Sec. IV D, we describe the application of pEMv2 to the population of TRAP-labeled Pma1 single particle trajectories. pEMv2 sorts TRAP-labeled Pma1 trajectories into two states. After analyzing the mean squared displacements of the sorted tracks in Sec. IV E, we test the sorted populations by comparing their covariance and diffusivity distributions to the corresponding theoretical distributions. We find good agreement between pEMv2-sorted covariance distributions and theory (Sec. IV F), bolstering the pEMv2-based approach. Similar analysis of a simulated population of tracks, that mimics experimental TRAP-labeled population (Sec. IV G) yields excellent agreement between theory and pEMv2-sorted covariance values. Next, in Sec. IV H, we analyze the population of Pma1-mEos3.2 direct fusion tracks with pEMv2, and find that it also shows two states. However, in contrast to TRAP-labeled Pma1, where the mobile fraction is about 0.5, the fraction of Pma1-mEos3.2 direct-fusion tracks in the mobile state that is 0.1. In addition to the much reduced mobile

fraction in Pma1-mEos3.2 compared to TRAP-labeled Pma1, the diffusivities of the mobile sub-populations alone appear to be different for the two labeling strategies with the mean diffusivity of the mobile sub-population of TRAP-labeled Pma1 ($D_2 \simeq 0.16 \mu\text{m}^2\text{s}^{-1}$) being several-fold larger than the mean diffusivity of the mobile state (state 2) of Pma1-mEos3.2 ($D_2 \simeq 0.05 \mu\text{m}^2\text{s}^{-1}$). Direct comparison between the sorted experimental diffusivity and covariance distributions with the theoretical diffusivity and covariance distributions from Refs. [18, 22] reveals good agreement between experiment and theory in this case too. Finally, in Sec. V, we summarize and conclude.

II. BACKGROUND

A. Pma1

Pma1 is the most abundant protein in the plasma membrane of budding yeast (*Saccharomyces cerevisiae*). It is a transmembrane protein which pumps protons out of the cell and thus plays a role in regulating the pH of the cytoplasm. Pma1 is also a marker of cell aging because, interestingly, there is less Pma1 in the plasma membranes of newly-budded daughter cells, than in the membranes of their mother cell [9]. The yeast plasma membrane is laterally organized into several different membrane “compartments” or domains. As the name implies, Pma1 is the majority protein component of the membrane compartment of Pma1 (MCP). Membrane compartments, including MCP, show characteristic linear dimensions of about $0.1 \mu\text{m}$ [5, 7], and differ from each other in their composition, size, shape, etc. [10] – MCPs are enriched in sphingolipids, as well as Pma1, and show non-compact, “network-like” shapes [7]. Pma1 contains 918 amino acids, comprising four domains: a membrane domain which includes ten transmembrane α -helices, a phosphorylation domain, a nucleotide-binding domain, and an actuator-domain, which experiences significant rearrangements when Pma1 cycles between the two allosteric states, activated and inhibited, involved in its enzymatic cycle. The change from Pma1’s inhibited to activated state has been proposed to be a consequence of phosphorylation of a specific Ser residue (Ser 899) and the tandem phosphorylation of a Ser/Thr pair (Ser911 and Thr912) [1, 2]. Recently, two cryo-electron microscopy studies of detergent-extracted, lipid-reconstituted, hexamerically-associated Pma1 (from *S. cerevisiae* and *Neurospora crassa*) provided microscopic details of the inhibited and activated molecular structures [11, 12]. Other studies involving *in vitro* reconstitution into liposomes [3] or nanodiscs [23] report that Pma1 monomers are active in proton pumping. As far as we are aware, no study has yet definitively identified the *in vivo* association state of Pma1.

B. TRAP labeling

Imaging fluorescently-labeled proteins continues to provide critical insights into the structure, organization and dynamics within living cells. The most widely-used live-cell labeling strategy is to replace the endogenous, “wild type” version of a protein of interest (POI) with a POI-fluorescent protein (POI-FP) fusion. In many cases, the assumption that the POI’s intrinsic biological function will be unaffected by the addition of the FP is surely correct. However, in some cases, adding an FP to a POI can cause the modified protein to mislocalize [24] or misfunction [25–28]. Pma1 provides an example of a protein that is sensitive to labeling method: Yeast strains expressing direct fusions of Pma1 and the FPs, mCherry or EGFP, both exhibit compromised growth and mislocalization of Pma1-mCherry or Pma1-EGFP, respectively, to the vacuole [15]. The possibility of mislocalization or misfunction of direct fusion proteins has motivated efforts to develop and deploy alternative *in vivo* labeling methods that are less disruptive of the protein’s localization or function [13–17].

Tetratricopeptide repeat affinity proteins (TRAPs) are notable for their ability to recognize and bind to 5-amino-acid peptide sequences. These binding reactions are reversible, and the TRAP-peptide pairs can be engineered to exhibit a range of binding affinities. In addition, TRAP-peptide pairs can readily be incorporated and utilized in live-cell systems. Capitalizing on these features, Ref. [13] developed TRAP-peptide pairs into a versatile imaging strategy for *in vivo* protein studies, in which each TRAP is genetically fused to a FP, while its cognate peptide is genetically fused to the C-terminus of the POI. Thus, the POI becomes fluorescently-labeled when the TRAP binds its cognate peptide on the POI. For brevity, throughout this paper, we call this labeling method “TRAP labeling”. Ref. [13] demonstrated the utility of TRAP labeling for imaging the cell division protein FtsZ in the bacteria, *Escherichia coli*, provided the binding affinity is sufficiently high. Ref. [16] further showed the method’s ability to enable super-resolution imaging in budding yeast, *Saccharomyces cerevisiae*.

C. Perturbation expectation maximization

A number of methods have been introduced for addressing particle tracks exhibiting biological heterogeneity [19, 20, 29–35]. In particular, Refs. [19, 20] describe *perturbation expectation maximization*, pEMv2, which simultaneously analyzes a population of particle trajectories and sorts the trajectories into distinct diffusive states, each with its own diffusion properties. pEMv2 is a machine-learning approach that makes no *a priori* assumptions concerning the character of a diffusive state—*e.g.* whether it corresponds to simple diffusion or not—but rather determines each state’s diffusive properties directly from the sorted tracks.

Although pEMv2 performs well on simulations, to date it has been applied to relatively few experimental data sets [20, 21]. Moreover, in pEMv2’s published experimental applications, it has found populations consisting of six or more diffusive states. To more robustly demonstrate the utility of pEMv2, and promote confidence in its results, it would be valuable to find an experimental application that involves just a few diffusive states, and explore pEMv2’s performance in this context, in particular, by comparing the statistical properties of pEMv2-sorted populations, which pEMv2 asserts are homogeneous, to theoretical expectations for a population of tracks with a single set of diffusion parameters [18, 22].

pEMv2 is described in detail in Refs. [19, 20]. In brief, it is an unsupervised, systems-level, machine-learning-based data analysis and classification method, that takes as input a heterogeneous population of single particle trajectories. It hypothesizes the existence of several different diffusive states within the population; it then determines the most likely diffusive properties of each diffusive state, while sorting each trajectory into the most likely of these diffusive states; it follows this procedure for different numbers of diffusive states, and finally picks the optimum number of diffusive states.

Specifically, for K diffusive states and M tracks, pEMv2 maximizes the log-likelihood of obtaining the measured tracks:

$$\log \mathcal{L} = \sum_{m=1}^M \log \left(\sum_{k=1}^K \pi_k P(\Delta \mathbf{x}_m, \Delta \mathbf{y}_m | \Sigma_k) \right), \quad (1)$$

where $\Delta \mathbf{x}_m$ is the vector of displacements along x for track m , $\Delta \mathbf{y}_m$ is the vector of displacements along y for track m , π_k is the fraction of tracks in diffusive state k , Σ_k is the displacement covariance matrix of diffusive state k (assumed the same for x and y), and

$$P(\Delta \mathbf{x}_m, \Delta \mathbf{y}_m | \Sigma_k) = \frac{e^{-\frac{1}{2} \Delta \mathbf{x}_m^T \Sigma_k^{-1} \Delta \mathbf{x}_m - \frac{1}{2} \Delta \mathbf{y}_m^T \Sigma_k^{-1} \Delta \mathbf{y}_m}}{(2\pi)^N |\Sigma_k|} \quad (2)$$

is the probability of realizing trajectory m , given that trajectory m corresponds to diffusive state k , with $|\Sigma_k|$ and Σ_k^{-1} the determinant and inverse of Σ_k , respectively. For trajectories comprising N displacements in x and y , each of $\Delta \mathbf{x}_m$ and $\Delta \mathbf{y}_m$ is an N -component vector and Σ_k is an $N \times N$ symmetric Toeplitz matrix. That is, pEMv2 assumes that particle displacements are multivariate Gaussian random variables. To apply pEMv2 to experimental tracks, we subdivide longer tracks into N step tracks. pEMv2 maximizes $\log \mathcal{L}$ iteratively by appropriately picking π_k and the matrix elements of Σ_k for each diffusive state k , and by assigning each track to the most likely diffusive state.

Model selection in pEMv2—that is, picking the appropriate value of K —is implemented by picking the state with the largest Bayesian Information Criterion (BIC), defined here as

$$\text{BIC} = \log \mathcal{L} - \frac{1}{2} N_P \log N_D, \quad (3)$$

where $N_D = 2NM$ is the number of data points, and $N_P = KN + K - 1$ is the number of model parameters, equal to the sum of the number of independent covariance matrix elements, KN , plus the number of independent population fractions, $K - 1$. The log-likelihood always increases as the number of parameters, and therefore the number of states, increases. Counteracting this behavior, the second term on the right hand side of Eq. 3 penalizes a larger number of parameters, and therefore a larger number of states. Together these two contributions lead to an optimum value of K .

D. Covariance and diffusivity distributions

According to pEMv2, its sorted populations each correspond to a single diffusive state with well-defined dif-

$$P(S_n|\Sigma) = \int d(\Delta x_1)\dots d(\Delta y_1)\dots P(\Delta x, \Delta y|\Sigma) \delta(S_n - \frac{1}{2}\Delta x^T C_n \Delta x - \frac{1}{2}\Delta y^T C_n \Delta y) = \int_{-\infty}^{\infty} \frac{d\omega}{2\pi} \frac{1}{|I + \frac{i}{2}\omega \Sigma C_n|} e^{i\omega S_n}, \quad (4)$$

where $[C_0]_{jk} = \frac{2}{N}I$ and $[C_n]_{jk} = \frac{1}{(N-n)}\delta_{j, k\pm n}$ for $n > 0$, where $j = 1$ through N .

Many experimental systems, including TRAP-labeled Pma1 and Pma1-mEos3.2, show diffusive behavior consistent with simple diffusion with experimental errors, corresponding to a symmetric, tridiagonal covariance matrix, where the only non-zero mean covariance matrix elements are on the diagonal, namely \bar{S}_0 , and one away from the diagonal, namely \bar{S}_1 . Each individual track yields a measurement of S_1 and S_0 , which are related to a measurement of the diffusivity, D , and the static localization

diffusive properties and parameters. Assuming that a given diffusive state's displacements are a zero-mean Gaussian random variable (Eq. 2), all statistical properties of the displacements are determined solely by the mean covariance matrix. Therefore, to test pEMv2's performance, we sought to compare the pEMv2-sorted covariance- and diffusivity-distributions to the corresponding theoretical expectations, given the experimental mean covariances.

The development of theoretical predictions for covariance- and diffusivity-distributions is described in detail in Refs. [18, 22]. In brief, for a population of two-dimensional, single-particle trajectories, each of length N , and each corresponding to the same diffusive state, the probability density for a track to yield an estimate of the covariance matrix element, n steps away from the diagonal, equal to S_n , is:

noise, σ^2 , for that track via [22]

$$S_0 = \sum_{j=1}^N (\Delta x_j^2 + \Delta y_j^2) = 4D\Delta t - \frac{4}{3}D\Delta t_E + 2\sigma^2 \quad (5)$$

and

$$S_1 = \sum_{j=1}^{N-1} (\Delta x_j \Delta x_{j+1} + \Delta y_j \Delta y_{j+1}) = \frac{2}{3}D\Delta t_E - \sigma^2, \quad (6)$$

where Δt is the time between camera exposures and Δt_E is the exposure time. The terms involving the exposure time, Δt_E , correspond to motion blur, because measurement of the particle position is integrated while the shutter is open. To be clear, S_0 , S_1 , D , and σ^2 are random variables. Their respective means are \bar{S}_0 , \bar{S}_1 , \bar{D} , and $\bar{\sigma}^2$.

Solving Eqs. 5 and 6 for D and rewriting in terms of C_0 , C_1 , $\Delta \mathbf{x}$ and $\Delta \mathbf{y}$, [18, 22], we find

$$D = \frac{S_0}{4\Delta t} + \frac{S_1}{2\Delta t} = \frac{1}{4\Delta t} (\Delta x^T C_0 \Delta x + \Delta y^T C_0 \Delta y) + \frac{1}{2\Delta t} (\Delta x^T C_1 \Delta x + \Delta y^T C_1 \Delta y). \quad (7)$$

Similarly,

$$\sigma^2 = \frac{\Delta t_E}{6\Delta t} S_0 + \left(\frac{\Delta t_E}{3\Delta t} - 1 \right) S_1 = \frac{\Delta t_E}{6\Delta t} (\Delta x^T C_0 \Delta x + \Delta y^T C_0 \Delta y) + \left(\frac{\Delta t_E}{3\Delta t} - 1 \right) (\Delta x^T C_1 \Delta x + \Delta y^T C_1 \Delta y). \quad (8)$$

It follows that the the probability densities of the diffusivity and the static localization

as

$$P(D|\Sigma) = \int_{-\infty}^{\infty} \frac{d\omega}{2\pi} \frac{1}{|I + \frac{i}{8\Delta t}\omega \Sigma (C_0 + 2C_1)|} e^{i\omega D}. \quad (9)$$

and

$$P(\sigma^2|\Sigma) = \int_{-\infty}^{\infty} \frac{d\omega}{2\pi} \frac{1}{|I + \frac{i}{2\Delta t} \omega \Sigma (\frac{\Delta t_E}{6\Delta t} C_0 + (\frac{\Delta t_E}{3\Delta t} - 1) C_1)|} e^{i\omega D}, \quad (10)$$

respectively. For each of Eq. 4, Eq. 9, and Eq. 10, to provide explicit results, we calculate the determinant in the integrand as a function of ω and then carry out each integral over ω numerically.

Eq. 4, Eq. 9, and Eq. 10 are applicable when there is one diffusive state. The generalization to K states, with population fractions specified by $\{\pi_k\}$ and diffusion properties specified by $\{\Sigma_k\}$, is straightforward:

$$P(S_n|\{\pi_k\}, \{\Sigma_k\}) = \sum_{k=1}^K \pi_k P(S_n|\Sigma_k), \quad (11)$$

$$P(D|\{\pi_k\}, \{\Sigma_k\}) = \sum_{k=1}^K \pi_k P(D|\Sigma_k), \quad (12)$$

and

$$P(\sigma^2|\{\pi_k\}, \{\Sigma_k\}) = \sum_{k=1}^K \pi_k P(\sigma^2|\Sigma_k), \quad (13)$$

where $\{..\}$ indicates “the set of ...”.

III. MATERIALS AND METHODS

A. Sample preparation

All measurements described in this paper employed strains of the budding yeast, *Saccharomyces cerevisiae*. The construction of these strains is described in detail in [15, 36]. For strains expressing a modified version of Pma1p, we replaced the native chromosomal PMA1 gene with a gene encoding modified Pma1p. Modified Pma1p was expressed from the endogenous PMA1 promoter, allowing us to study behavior at endogenous expression levels.

For our microscopy experiments, overnight cultures were grown in synthetic defined (SD) media, with 2% sucrose and 1% raffinose. These starter cultures were diluted into fresh media, containing 2% galactose, to obtain a final $OD_{600} \approx 0.05$. Growth was then continued at 30°C for a further 8 hrs. Cells from these cultures were then imaged as follows: 1 mg/mL of concanavalin A (conA) was applied to a clean cover slip, and incubated at room temperature for 10 minutes. Then, 0.5-1.0 mL of fresh milli-Q water was used to rinse off the excess conA. Next, the yeast culture, previously vortexed for approximately 30 s to separate any cell clusters, was added to the conA-coated cover slip and incubated at room temperature for an additional 10 minutes. Excess, unbound cells were rinsed from the cover slip, which was then sealed to a microscope slide using a 1:1:1 ratio mixture of Vaseline, lanolin and paraffin wax (VALAP).

	TRAP-peptide-labeled Pma1	Pma1-mEos3.2
Number of cells studied	14	20
Number of tracks	59226	20253
Number of movie frames	60000	60000

TABLE I. Number of cells, number of tracks (defined by two or more steps), and number of movie frames for the two strains imaged under TIRF conditions.

B. Microscopy

Microscopy measurements to track the motions of individual molecules of TRAP-labeled Pma1 and Pma1-mEos3.2 were carried out using the custom-built microscope, described in Ref. [37], which has both total-internal reflection fluorescence (TIRF) and photo-activation localization microscopy (PALM) capabilities. We employed a 405 nm-wavelength laser to switch mEos3.2 into its red state and a 560 nm-wavelength laser for imaging of switched mEos3.2. As noted previously, Pma1 is the most abundant yeast membrane protein. Therefore, switching a subset of the population into mEos3.2’s red fluorescent state ensures sufficiently isolated, and therefore resolvable, individual trajectories for Pma1-mEos3.2, that are suitable for unambiguous single particle tracking. The trajectories reported and analyzed in this paper were collected under conditions of TIRF illumination, which restricted switching and fluorescence excitation to the portion of a cell’s membrane in close proximity to the coverslip. In addition, however, a limited quantity of wide-field PALM data were collected to visually assess the extent to which PALM signal is associated with the cell membrane. The intensity of the 405 nm-wavelength laser was manually adjusted during the experiments to ensure a sufficient signal rate throughout the duration of data acquisition. The fields-of-view imaged were 256×256 pixels, with square pixels, each spanning 103 nm on a side. Images were collected at a rate of 100 frames per second (fps), corresponding to $\Delta t = 0.01$ s. The exposure time was also $\Delta t_E = 0.01$ s. A custom, reflection-based autofocus system was deployed during data acquisition to maintain the microscope focus.

C. Single particle tracking

Single particle tracking was accomplished using a locally-customized Matlab version (The MathWorks, Inc.) of the software, described in Ref. [38], initially resulting in a number of candidate localizations in each movie frame. To achieve our final set of localizations, we manually segmented brightfield images to find cells and excluded any (apparent) localizations outside cells.

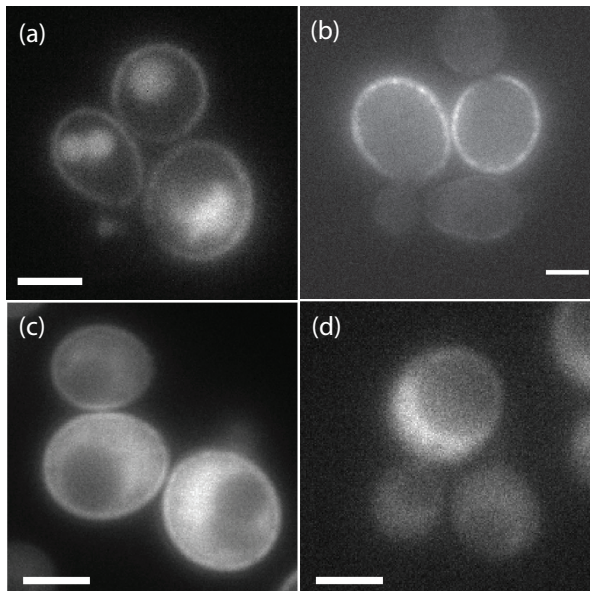


FIG. 1. Wide-field fluorescence microscopy images for four strains of *S. cerevisiae*: (a) Cells expressing the Pma1-mCherry direct fusion; (b) Cells expressing the Pma1-mEos3.2 direct fusion; (c) Cells expressing the Pma1-MEEVF/TRAP-mEos3.2 TRAP-peptide system; and (d) Cells expressing untagged Pma1 and TRAP-mEos3.2. In each case, the scale bars correspond to 3 μm .

We also excluded localizations with standard deviations less than 0.5 pixels or more than 3.5 times the mean standard deviation of the population of localizations. Finally, to construct single-particle trajectories, spanning multiple movie frames—*i.e.* spanning time—we insisted that the maximum number of pixels that a particle can move between successive frames is 2 pixels, and that the maximum number of frames for which a particle can transiently disappear and still be considered part of a specific trajectory is 1 frame.

D. Simulations

Populations of simulated trajectories were generated as described in Ref. [20]. In brief, first, tracks undergoing normal diffusion were generated according to:

$$x(i+1) = x(i) + [2D\Delta t_S \delta_{i,j}]^{\frac{1}{2}} W(j) \quad (14)$$

where $x(i)$ is the x -coordinate of the particle's position at time step i , $x(0) = 0$, $W(j)$ is a standard Brownian motion with $\langle W(j) \rangle = 0$ and $\langle W(j)W(j) \rangle = \delta_{i,j}$, and $\Delta t_S = \frac{1}{32} \Delta t_E$ is the simulation time step. We then averaged over blocks of 32 simulation time steps, thus achieving a simulated motion-blurred trajectory with successive positions, separated in time by the experimental exposure time. Finally, we added Gaussian-distributed localization noise to each position in the motion-blurred trajectory.

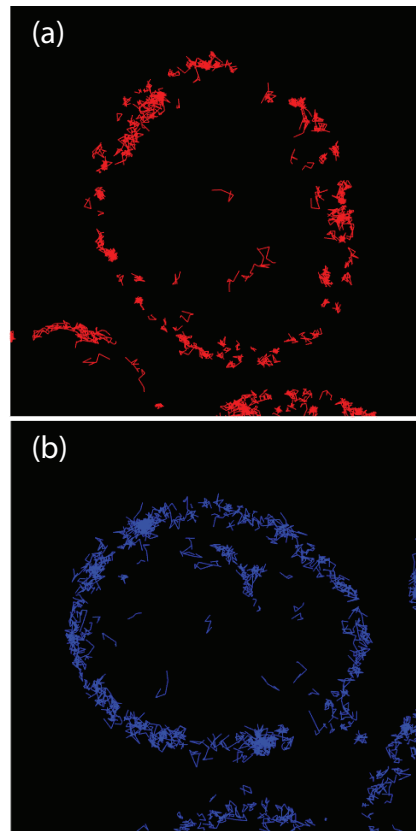


FIG. 2. Trajectories comprising four or more steps obtained from 20000 frames of wide-field PALM movies from cells with (a) Pma1-mEos3.2 and (b) TRAP-labeled Pma1.

IV. RESULTS AND DISCUSSION

A. Microscopy

Fig. 1(a) shows wide-field fluorescence microscopy images of cells expressing a Pma1-mCherry direct fusion. Apparent in this image is a bright halo of fluorescence intensity at the cell periphery, corresponding to the localization of Pma1-mCherry to the cell membrane. Also apparent in this image is fluorescence intensity originating from regions inside the cell, corresponding to mislocalization of Pma1-mCherry to vacuoles. Evidently, the fusion of mCherry to Pma1 causes Pma1's behavior to diverge significantly from its intrinsic behavior, which does not involve localization to vacuoles. Fig. 1(b) shows cells expressing a Pma1-mEos3.2 direct fusion. In this case also, there is a halo of fluorescence intensity at the cells' periphery, corresponding to the localization of Pma1-mEos3.2 to the cell membrane. However, in this case, there is no mislocalization to vacuoles. Fig. 1(c) shows cells with TRAP-labeled Pma1, *i.e.* cells expressing both Pma1-MEEVF and TRAP-mEos3.2. In this case too, there is a halo at the cell membrane, indicating the presence of the Pma1-MEEVF-TRAP-mEos3.2 complex localized to the membrane, consistent

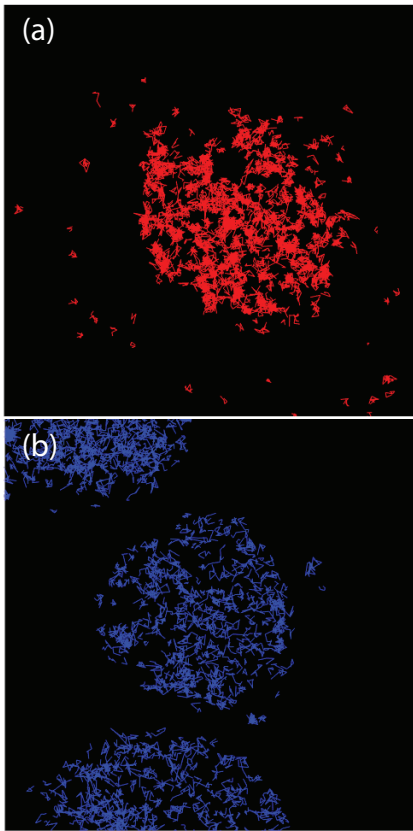


FIG. 3. Trajectories comprising four or more steps obtained from 20000 frames of PALM movies, under TIRF illumination, from cells with (a) Pma1-mEos3.2 and (b) TRAP-labeled Pma1.

with strong MEEVF-TRAP binding, for which Ref. [13] estimated the dissociation constant to be $K_D \simeq 300$ nM. In Fig. 1(c), fluorescence intensity also originates within the cell, corresponding to free TRAP-mEos3.2 in solution. Finally, Fig. 1(d) shows cells expressing TRAP-mEos3.2 but with unmodified Pma1. As expected, there is no longer an intensity halo at the cells' periphery, because the TRAP-mEos3.2's MEEVF binding partner is absent from Pma1 or anywhere else.

For the images in Fig. 1(b-d), mEos3.2 was visualized through its unswitched green fluorescence. However, mEos3.2 can be switched by exposure to 405 nm wavelength light into a red fluorescent state. Fig. 2 depicts trajectories of switched, red-emitting proteins containing four or more steps obtained from movies collected under 565-nm-illumination from cells with (a) Pma1-mEos3.2 and (b) TRAP-labeled Pma1. In both cases, the spatial distribution of trajectories clearly outlines the periphery of the cell that intersects the focal plane. There is no obvious difference in the spatial distribution of the tracks obtained for Pma1-mEos3.2, which we expect to be strictly confined to the cell membrane, and tracks obtained for TRAP-labeled Pma1. Initially, it may seem surprising that there are no trajectories corresponding to the cytoplasmic fluorescence apparent in Fig. 1(c), which

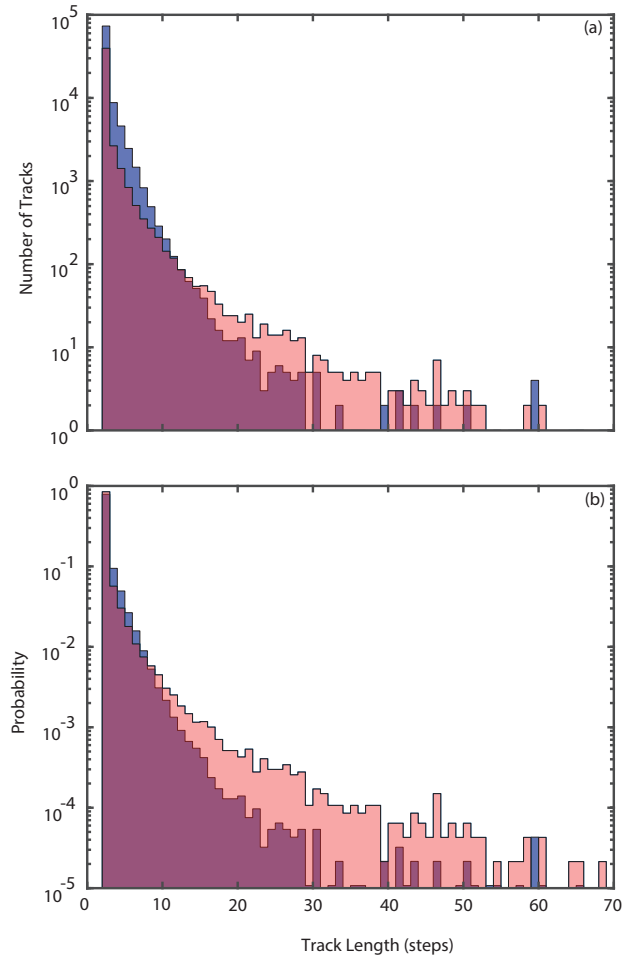


FIG. 4. (a) Number of tracks and (b) probability versus track length plotted on logarithmic-linear axes for TRAP-labeled Pma1, shown in blue, and Pma1-mEos3.2, shown in pink. Two is the minimum number of connected steps to be considered a track.

depicts the same yeast strain as Fig. 2(b). However, we expect that an unbound TRAP-mEos3.2, freely and rapidly diffusing in the cytosol, would yield either a localization in just a single movie frame or a very short track at most. We infer, therefore, that trajectories with four or more steps in cells with TRAP-peptide labeling overwhelmingly must correspond to labeled Pma1 in the cell membrane, and not to unbound MEEVF-mEos3.2 in the cytosol.

More generally, the observation that unbound TRAP-mEos3.2 may be eliminated from consideration by insisting on sufficiently long tracks suggests a possible general strategy for *imaging* TRAP-labeled POIs [14, 39], namely to insist that tracks endure for some minimum number of time steps. In this case, the fluorescence from unbound TRAP-FPs may be less of a problem for imaging than it might originally have seemed.

Fig. 3 shows trajectories also containing four or more steps, obtained from PALM movies collected with TIRF

illumination, from cells with (a) Pma1-mEos3.2 and (b) TRAP-labeled Pma1. For both labeling methods, tracks appear largely confined to roughly circular regions. Because the tracks are derived from TIRF data, so that we expect to visualize only tracks close to the cover slide, we identify each roughly-circular region as the area of the cell in contact with the cover slide. Apparent tracks outside these regions were eliminated from further consideration. Because all of these trajectories involve four or more steps and because they were acquired through TIRF, we are confident that overwhelmingly they correspond to TRAP-labeled Pma1 and not freely-diffusing TRAP-mEos3.2. Although wide-field PALM measurements were important for establishing the conditions necessary to examine TRAP-labeled Pma1, in the remainder of the paper, we focus solely on the two-dimensional trajectories collected with TIRF illumination, in order to avoid any ambiguities associated with the sideways view of membrane-based trajectories acquired in wide-field.

B. Distribution of track lengths

Fig. 4 displays the number of tracks versus track length on linear-logarithmic axes for both TRAP-labeled Pma1 (blue) and Pma1-mEos3.2 (pink). Evidently, for both labeling methods, the number of tracks is a monotonically decreasing function of the number of steps in the track. The track length distribution is equivalent to the distribution of fluorescent state lifetimes, because the product of the number of steps in a track and duration of a step corresponds to the lifetime of the corresponding FP(s). The behavior of lifetime distribution clearly indicates that each of the observed tracks corresponds to a single FP, *i.e.*, these are monomer tracks. In contrast to the observations, the lifetime distribution for a protein complex, which includes several FPs moving together, is expected to start at zero, then increase to a peak at non-zero time, before decreasing to zero again at large times. This prediction is readily understood in the case of a monomer lifetime distribution given by $\lambda e^{-\lambda t}$ – a simple exponential with a characteristic rate, λ . Then, for an n -mer comprising n independent monomers, the lifetime distribution is readily shown to be $n\lambda e^{-\lambda t}(1 - e^{-\lambda t})^{n-1}$. With increasing t , this n -mer lifetime distribution indeed starts at zero at $t = 0$, then increases to a peak at $t = \frac{\log n}{k}$, before decreasing to zero again at large times, as advertized.

Although the tracks of both TRAP-labeled Pma1 and Pma1-mEos3.2 correspond to monomers, there is nevertheless a clear difference in the track length distribution between the two methods with the direct fusion showing more long tracks than TRAP-labeled Pma1. This observation is consistent with the interpretation that when Pma1 is directly bound to the FP, the lifetime of the signal is limited by photobleaching, whereas when Pma1 is labeled by the TRAP-peptide pair, the lifetime is limited by a combination of photobleaching and the lifetime of

TRAP-MEEVF binding. Thus, we expect shorter lifetimes for TRAP-labeled Pma1 than for Pma1-mEos3.2. In fact, the normalized distribution of TRAP-labeled Pma1 track lengths (Fig. 4(b)) falls a factor of e below that of Pma1-mEos3.2 for a track length of about 15, suggesting that the mean lifetime of the MEEVF-TRAP bond is about 0.15 s. Equivalently, the MEEVF-TRAP unbinding rate is about 6 s^{-1} .

C. Population-averaged diffusivity distributions

Fig. 5 compares population-averaged, diffusivity distributions, calculated on the basis of Eq. 7, for (a) the population of TRAP-labeled Pma1 tracks, (b) simulated TRAP-labeled Pma1 tracks, and (c) the population of Pma1-mEos3.2 tracks. In the figure, the overall diffusivity distributions of these populations are shown as the light-grey histograms. Although both protein variants' overall diffusivity distributions are peaked near zero, the Pma1-mEos3.2's diffusivity distribution is largely confined within $\pm 0.1 \mu\text{m}^2/\text{s}$. By contrast, TRAP-labeled Pma1's diffusivity distribution shows a large diffusivity tail, extending beyond $0.5 \mu\text{m}^2/\text{s}$. Evidently, a substantial, qualitative difference between the overall diffusivity distribution of Pma1-mEos3.2 exists. and the diffusivity distribution of TRAP-labeled Pma1. This result shows directly, without any further detailed analysis, that labeling strategy significantly affects the dynamics of membrane-bound Pma1, with unknown consequences to Pma1's biological roles. Because TRAP-labeling minimally modifies the protein of interest, and direct fusions with other fluorescent proteins causes growth defects and Pma1 mislocalization, our assumption is that TRAP-labeled Pma1 more closely represents the intrinsic biological behavior of wild-type Pma1, than does Pma1-mEos3.2.

D. pEMv2 sorts TRAP-labeled Pma1 trajectories into two diffusive states

pEMv2 is most reliable for a large number of long trajectories [20]. By contrast, experimentally, as illustrated in Fig. 4, the number of available tracks decreases rapidly with increasing track length. Therefore, to explore pEMv2's performance and consistency over the range of available track lengths and numbers of tracks, we chose to partition each dataset into populations of trajectories with track lengths of 5, 6, 7, 8, 9, 10, 11, 12, and 15 steps. For the entire population of tracks, we find that the mean covariances, \bar{S}_n , are very close to zero for all $n > 1$ for all track lengths. Therefore, for simplicity we chose to set these covariances identically equal to zero when running pEMv2. The statement that $\bar{S}_n = 0$ for $n > 1$ is equivalent to the statement that labeled Pma1 undergoes simple diffusion in the presence of experimental errors.

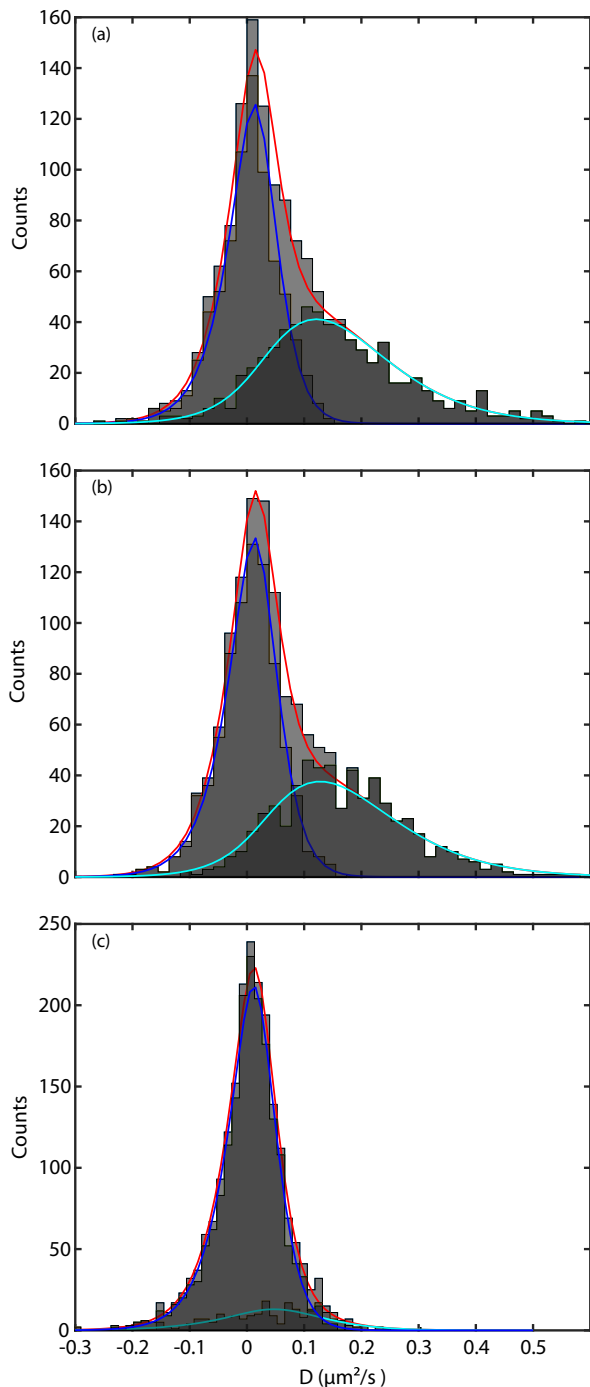


FIG. 5. Comparison between the distributions of diffusivities, D , for (a) experimental TRAP-labeled Pma1, (b) simulated TRAP-labeled Pma1 tracks, and (c) experimental direct fusion data. In all three cases, the track length equals 9 steps. The overall, unsorted, population-averaged distributions, shown as the light grey histograms, are plotted with the theoretical two-component curve, shown as the red curve, calculated using Eq. 12 and the pEMv2-found covariance values. The sorted diffusivity distributions (dark and darker grey histograms) are shown with their corresponding single state theory curves (blue and cyan curves), given by Eq. 9.

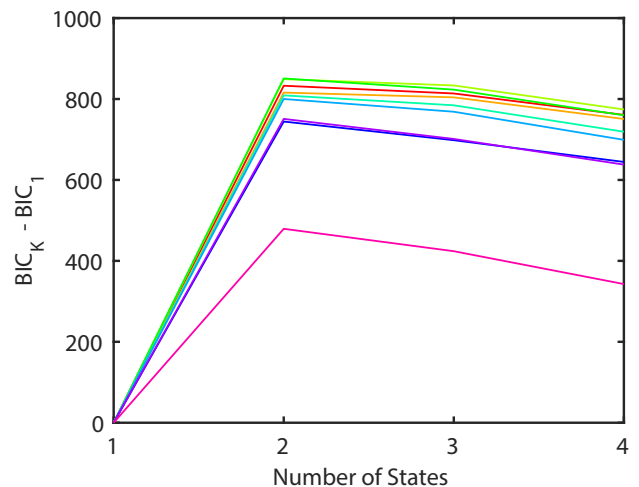


FIG. 6. Relative Bayesian Information Criterion ($BIC_K - BIC_1$) values versus number of diffusive states for TRAP-labeled Pma1 trajectories of length 5 (red), 6 (orange), 7 (lime green), 8 (green), 9, (blue-green), 10 (blue), 11 (dark blue), 12 (purple), and 15 (magenta). The highest relative BIC value for each track length occurs for two states, irrespective of track length.

We carried out a pEMv2-analysis for each population of different-length trajectories. Fig. 6 plots the values of $BIC_K - BIC_1$ returned by pEMv2 versus the number of diffusive states, K , for track lengths of 5, 6, 7, 8, 9, 10, 11, 12 and 15 steps. For each track length, the BIC achieves a maximum for $K = 2$, irrespective of track length, indicating that pEMv2 robustly supports two subpopulations, namely state 1 and state 2 – with distinct diffusive properties.

Table II reports the mean covariances, \bar{S}_0 and \bar{S}_1 , the mean diffusivity, \bar{D} and the mean localization noise for these two diffusive states, as well as the fraction of the population corresponding to state 1, ϕ_1 , the fraction of the population corresponding to state 2, ϕ_2 . Evidently, pEMv2 indicates the existence of a relatively low diffusivity state (state 1) with $D_1 \simeq 0.003 \mu\text{m}^2\text{s}^{-1}$ and a relatively high diffusivity state (state 2) with $D_2 \simeq 0.16 \mu\text{m}^2\text{s}^{-1}$, for a track length of 9 steps. Both states have roughly equal representation in the overall population with $\phi_1 \simeq 0.54$ and $\phi_2 \simeq 0.46$.

Table II reveals that the diffusivity of state 2, returned by pEMv2, decreases as the track length increases. We hypothesize that this circumstance arises because for increasing track length, high diffusivity tracks have a progressively higher probability to diffuse out of the illuminated volume than lower diffusivity tracks. Thus, a population of longer tracks is preferentially depleted of high-diffusivity tracks, pulling down the population's mean diffusivity, compared to a population of shorter tracks.

Track Length	\bar{S}_0	$\bar{S}_{0_{err}}$	\bar{S}_{11}	$\bar{S}_{02_{err}}$	D_1	$D_{1_{err}}$	σ_1^2	$\sigma_{1_{err}}^2$	\bar{S}_0	$\bar{S}_{02_{err}}$	\bar{S}_{12}	$\bar{S}_{12_{err}}$	D_2	$D_{2_{err}}$	σ_2^2	$\sigma_{2_{err}}^2$	ϕ_1	ϕ_2
5	0.0065	5.79×10^{-5}	-0.0032	5.10×10^{-5}	0.0013	0.0015	0.0032	4.27×10^{-5}	0.0124	8.72×10^{-5}	-0.0013	8.58×10^{-5}	0.2462	0.0041	0.0029	6.33×10^{-5}	0.57	0.43
6	0.0061	6.52×10^{-5}	-0.0030	5.55×10^{-5}	0.0053	0.0016	0.0030	4.67×10^{-5}	0.0118	9.39×10^{-5}	-0.0017	9.10×10^{-5}	0.2072	0.0042	0.0031	6.83×10^{-5}	0.53	0.47
7	0.0057	7.58×10^{-5}	-0.0028	6.27×10^{-5}	0.0023	0.0018	0.0028	5.31×10^{-5}	0.0110	1.04×10^{-4}	-0.0019	9.42×10^{-5}	0.1808	0.0044	0.0031	7.14×10^{-5}	0.48	0.52
8	0.0057	8.38×10^{-5}	-0.0027	6.64×10^{-5}	0.0081	0.0019	0.0027	5.64×10^{-5}	0.0108	1.29×10^{-4}	-0.0018	1.12×10^{-4}	0.1784	0.0053	0.0030	8.57×10^{-5}	0.54	0.46
9	0.0055	9.51×10^{-5}	-0.0027	7.28×10^{-5}	0.0033	0.0020	0.0027	6.26×10^{-5}	0.0104	1.46×10^{-4}	-0.0020	1.23×10^{-4}	0.1592	0.0055	0.0031	9.66×10^{-5}	0.54	0.46
10	0.0051	9.47×10^{-5}	-0.0024	7.20×10^{-5}	0.0071	0.0021	0.0024	6.18×10^{-5}	0.0102	1.62×10^{-4}	-0.0022	1.35×10^{-4}	0.1436	0.0062	0.0032	1.05×10^{-4}	0.54	0.46
11	0.0051	1.02×10^{-4}	-0.0024	7.49×10^{-5}	0.0081	0.0022	0.0024	6.47×10^{-5}	0.0102	1.89×10^{-4}	-0.0025	1.60×10^{-4}	0.1304	0.0069	0.0034	1.26×10^{-4}	0.61	0.39
12	0.0050	1.06×10^{-4}	-0.0023	7.35×10^{-5}	0.0090	0.0021	0.0024	6.43×10^{-5}	0.0103	2.15×10^{-4}	-0.0027	1.71×10^{-4}	0.1238	0.0068	0.0035	1.39×10^{-4}	0.63	0.37
15	0.0049	1.30×10^{-4}	-0.0024	8.80×10^{-5}	0.0036	0.0022	0.0024	7.81×10^{-5}	0.0090	2.68×10^{-4}	-0.0024	1.91×10^{-4}	0.1047	0.0079	0.0031	1.57×10^{-4}	0.73	0.27

TABLE II. Results from applying pEMv2 for TRAP-labeled Pma1 data: covariances (\bar{S}_0 and \bar{S}_1), diffusivities (D), localization errors (σ^2), and volume fractions (ϕ) for the two states found by pEMv2 for track lengths of $N = 5, 6, 7, 8, 9, 10, 11, 12$, and 15.

E. Mean-square displacements (MSDs) versus delay time of pEMv2-sorted trajectories

In Sec. IV D, we used the pEMv2-determined mean covariances to estimate the diffusivity of each diffusive state. Ref. [22] showed that such covariance-based estimators are statistically optimal. However, another widely-used means of characterizing diffusivity is via the slope of the mean-square displacement (MSD) versus time delay, which is a linear function for simple diffusion. Fig. 7(a) plots the mean-square MSDs for TRAP-labeled Pma1 trajectories for each state versus the number of steps. The MSDs for tracks corresponding to state 1 are shown in blue, while the MSDs for tracks corresponding to state 2 are shown in cyan. Evidently, the MSDs for state 1 are conspicuously constant versus time. This observation emphasizes that state 1 really is essentially immobile. By contrast, it is clear that the state-2 MSDs increase approximately linearly versus time, consistent with what is expected for simple diffusion. It is also apparent that the slopes of the state-2 MSDs tend to decrease with increasing track length, corresponding to an apparently decreasing diffusivity with increasing track length, mirroring the behavior observed for the covariance-based estimates of the diffusivity.

F. Covariance distributions of pEMv2-sorted TRAP-labeled Pma1 trajectories agree with theory

To further assess the performance of pEMv2, we first sought to compare the theoretical covariance distributions for each state, conditioned on their respective experimental mean covariances, \bar{S}_0 and \bar{S}_1 , to the corresponding experimental distributions. Such comparisons are presented in Fig. 8, Fig. 9, and Fig. 10, which plot both experimental and theoretical covariance distributions for 5-step, 9-step, and 15-step trajectories, respectively, sorted into states 1 and 2 and for the overall population of unsorted trajectories. Stepped histograms represent the experimental covariance distributions. Smooth lines are the theoretical covariance distributions with blue and cyan corresponding to the distributions (Eq. 4) for state 1 and state 2, respectively, and red corresponding to the two-component distribution (Eq. 11) for the overall, unsorted population. In all cases, the theory and

experiment appear to be in good agreement, despite the fact that no fitting is involved: The only input for the theoretical curves in these figures are the experimental mean values of \bar{S}_0 and \bar{S}_1 . The fact that the distributions to emerge from the pEMv2-sorted populations agree well with what is expected theoretically, without any fitting, strongly supports that pEMv2 is correctly characterizing the diffusive behavior of TRAP-labeled Pma1.

We also directly fit the unsorted covariance distributions to Eq. 11 with fitting parameters \bar{S}_0 , \bar{S}_1 , \bar{S}_0 , \bar{S}_1 , \bar{S}_0 , \bar{S}_1 , ϕ_1 , and ϕ_2 . ϕ_1 and ϕ_2 represent the fraction of tracks in states 1 and 2, respectively. Again, we took $\bar{S}_n = 0$ for $n > 1$. The black dashed lines in Fig. 8, Fig. 9, and Fig. 10 are the resultant best-fits. In each case, these fits closely outline the experimental distributions, and lead to similar covariance values and population fractions as pEMv2, although the best-fit values of \bar{S}_0 for both states are consistently slightly smaller for the fits than determined by pEMv2 and fitting assigns correspondingly more weight to state 2 than pEMv2 in order to maintain the mean of the overall covariance distribution (Fig. 11).

As discussed in Sec. II D, in the case of simple diffusion, we can re-cast the S_0 - and S_1 -distributions as diffusivity and localization noise distributions. Fig. 5(a) shows the distribution of diffusivities determined from 9-step trajectories for TRAP-labeled Pma1. The sorted diffusivity distributions (dark and darker grey histograms) are shown with their corresponding theory curves (blue and cyan curves), given by Eq. 9. The overall, unsorted diffusivity distributions, shown as the light grey histogram, may be compared to the theoretical two-component curve, shown in red, calculated using Eq. 12, using the covariance values from pEMv2. In each case, the theory curves agree well with the experimental distributions, without any fitting involved, again bolstering the idea that pEMv2 correctly sorts individual particle trajectories into two diffusive states with different diffusivities. The diffusivities and localization noises of state 1 and state 2 for each track length are included in Table II. Evidently, the diffusivity of state 1 is very small ($D_1 \simeq 0.005 \mu\text{m}^2\text{s}^{-1}$), rendering state 1 essentially immobile. By contrast, the diffusivity of state 2 ($D_2 \simeq 0.15 \mu\text{m}^2\text{s}^{-1}$) is much larger. In comparison to D_2 , Ref. [40], for example, estimates the diffusivity of membrane proteins in *Escherichia coli* to lie in the range $0.02 - 0.2 \mu\text{m}^2\text{s}^{-1}$, depending on the pro-

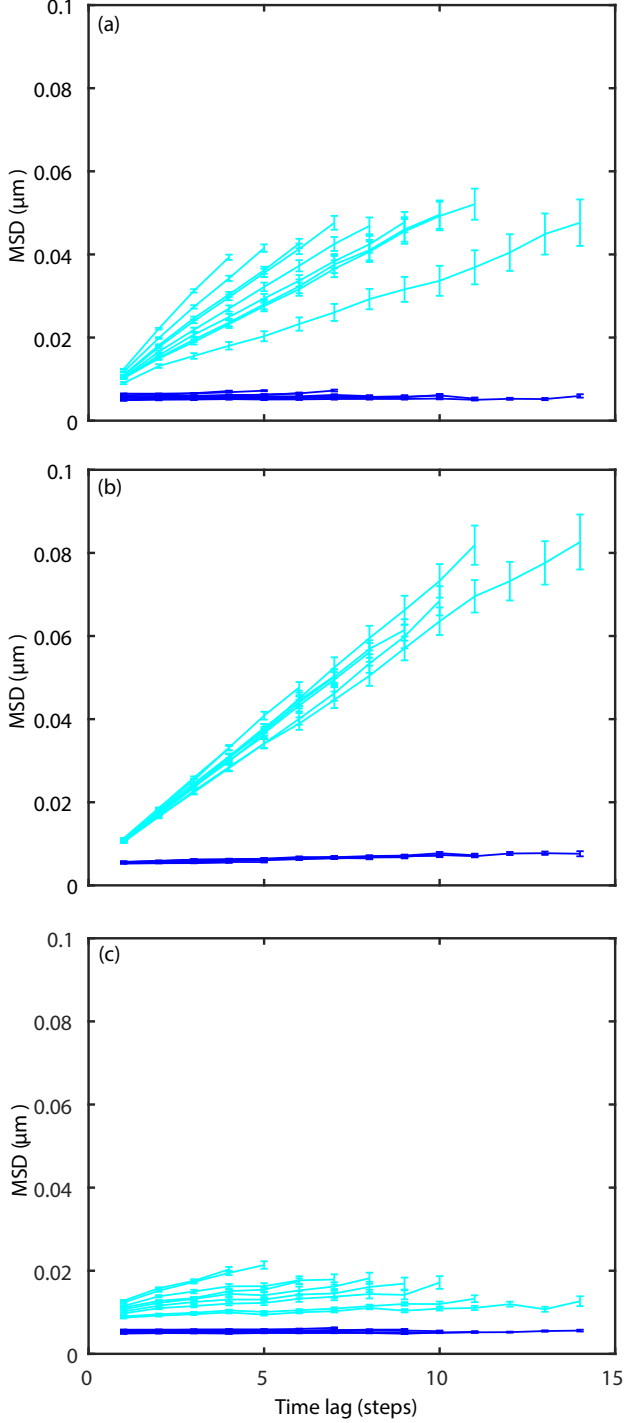


FIG. 7. Comparison of the mean squared displacements (MSDs) for state 1 (blue) and state 2 (cyan) across varying track lengths, for experimental TRAP-labeled Pma1 (a), simulated TRAP-labeled Pma1 (b), and experimental direct fusion data (c). In each case, the state 2 MSDs have higher slopes than state 1.

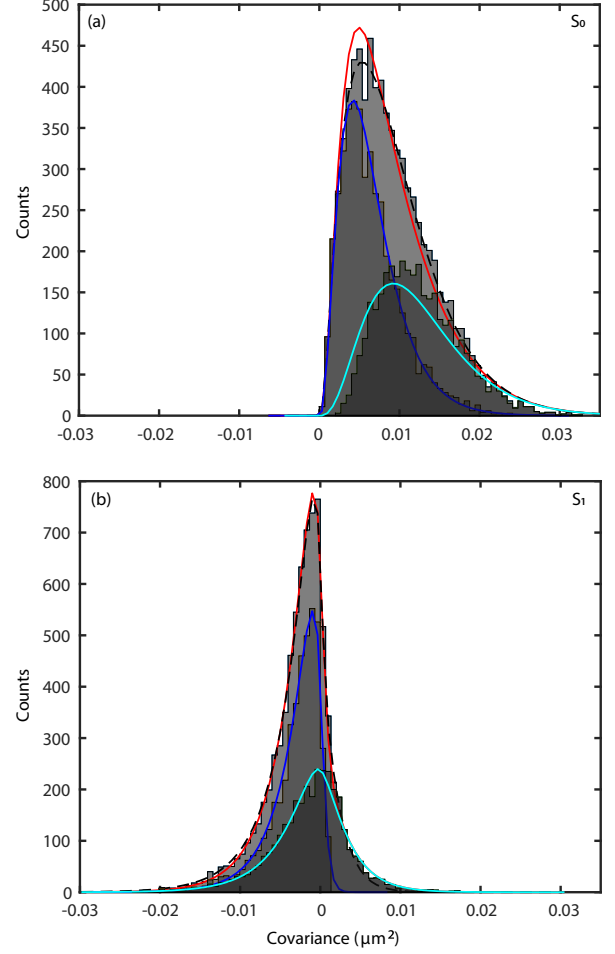


FIG. 8. Distribution of covariance elements (a) S_0 and (b) S_1 , for experimental 5-step TRAP-labeled Pma1 tracks. The unsorted covariance distribution (light grey histogram) is plotted with the theoretical two-component curve (red curve) given by Eq. 11, and the fitted two-component curve (black dashed line). The tracks are sorted into two distributions representing the two distinct diffusive states found by pEMv2 (dark grey and darker grey histograms), and plotted with their single theory curves (blue and cyan curves), given by Eq. 4.

tein in question. In the previous applications of pEMv2, Ref. [19] reports diffusivities of the proteins RhoA and RhoC in mammalian cell membranes in the range from $0.0002 - 0.7 \mu\text{m}^2\text{s}^{-1}$, while Ref. [21] reports diffusivities of WASP proteins in the range $0.01 - 0.8 \mu\text{m}^2\text{s}^{-1}$ also in mammalian cell membranes. Thus, the diffusivity of the mobile state of TRAP-labeled Pma1 (state 2) lies within the range expected for membrane proteins.

To further quantitatively compare the pEMv2-sorted experimental distributions and theory, we adopted a simulation-based approach to estimate the p-values appropriate to our measured distributions. Our p-values are defined to be the probability of realizing a certain

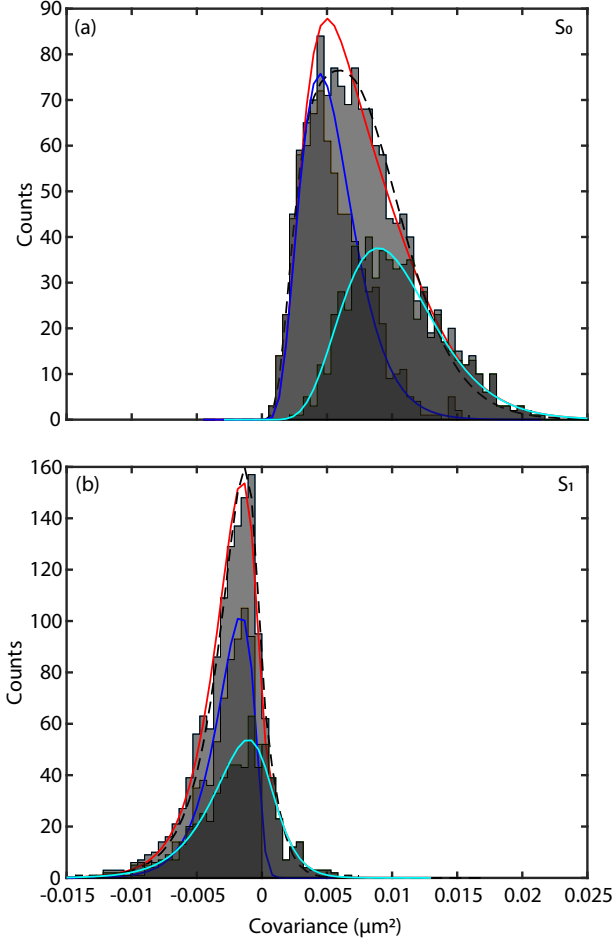


FIG. 9. Distribution of covariance elements (a) S_0 and (b) S_1 , for experimental 9-step TRAP-labeled Pma1 tracks. The unsorted covariance distribution (light grey histogram) is plotted with the theoretical two-component curve (red curve) given by Eq. 11, and the fitted two-component curve (black dashed line). The tracks are sorted into two distributions representing the two distinct diffusive states found by pEMv2 (dark grey and darker grey histograms), and plotted with their single theory curves (blue and cyan curves), given by Eq. 4.

test statistic that is greater than or equal to the value of that test statistic measured experimentally. The test statistic in question is the Kolmogorov-Smirnov statistic (KS statistic), equal to the maximum absolute difference between experimental and simulated cumulative distribution functions (CDFs) of the covariances. For each track length, we first simulated 40000 trajectories, far more than the number of experimental trajectories for any track length. The resultant simulated covariance distributions closely match the corresponding theoretical distributions with relatively small statistical errors. We used these 40000-trajectory-based distributions to determine an experimental KS-statistic, equal to the maximum absolute difference between the CDF of the exper-

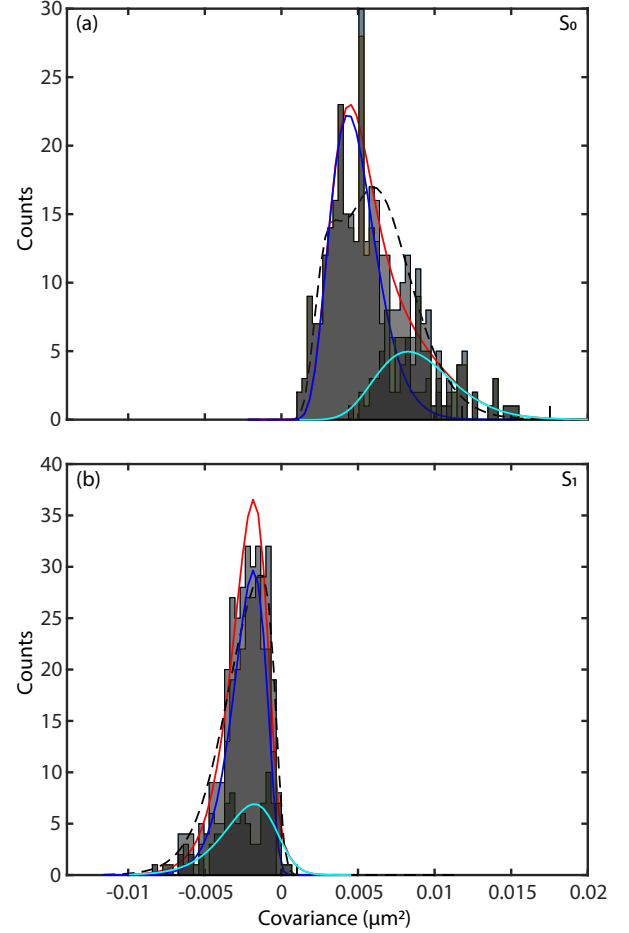


FIG. 10. Distribution of covariance elements (a) S_0 and (b) S_1 , for experimental 15-step TRAP-labeled Pma1 tracks. The unsorted covariance distribution (light grey histogram) is plotted with the theoretical two-component curve (red curve) given by Eq. 11, and the fitted two-component curve (black dashed line). The tracks are sorted into two distributions representing the two distinct diffusive states found by pEMv2 (dark grey and darker grey histograms), and plotted with their single theory curves (blue and cyan curves), given by Eq. 4.

imental covariance and the CDF of the covariance from the 40000-trajectory simulation. A single simulation of a number of trajectories equal to the number of experimental trajectories, together with the 40000-trajectory-based distribution, determines one simulated value of this KS statistic. To determine the cumulative distribution function of this KS statistic, we repeated such a simulation 2000 times for each track length, yielding 2000 values of the KS statistic for each track length. Then, the probability of realizing a KS statistic, greater than or equal to the experimental value—*i.e.* the p-value of the experimental KS statistic—can then be read from a plot of one minus the CDF of the KS statistic versus KS statistic. Fig. 12 displays the p-value so-obtained versus KS statistic for each diffusive state, for each track length, and

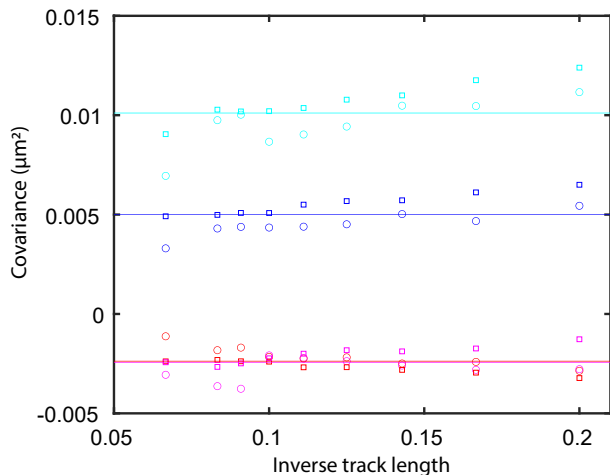


FIG. 11. Plot comparing the fitted S_0 and S_1 values (circles) to the pEMv2 found values (squares), versus inverse track length, for experimental TRAP-labeled Pma1. The S_0 values are in blue and cyan for states 1 and 2, respectively. The S_1 values are in red and magenta for states 1 and 2, respectively. Solid lines represent guides to the data, and are calculated by taking the average of the S values for each state over the track lengths.

for each of S_0 and S_1 . In addition, highlighted in this figure are the corresponding experimental KS statistics and their corresponding p-values, shown as black circles. Fig. 13 replots the p-value curves of Fig. 12 as a function of $\sqrt{\frac{n_1 n_2}{n_1 + n_2}} \times \text{KS statistic}$, where $n_1 = 40000$ and n_2 is the relevant number of experimental tracks. Evidently, plotted in this way, all of the curves more-or-less collapse onto each other. In fact, according to the Kolmogorov theorem, in the large- n_1 , large n_2 limit, the p-value plotted in this way for a one-dimensional probability distribution is a universal function, namely the Kolmogorov distribution, independent of the distribution of the underlying random variables. This prediction appears to be closely followed for our values of n_1 and n_2 .

The KS statistics and p-values are presented for multiple track lengths in Table III. For each of eighteen S_1 -distributions, in every case, the estimated p-value is larger than 0.05, indicating that in every case, the experimental S_1 -distribution closely matches the expected distribution. However, in spite of apparent good theory-experiment agreement in Fig. 8 for a track length of $N = 5$ steps, for the state-2 S_0 -distributions for $N = 5$ and 6 steps, the experimental KS statistics fall outside of the range of simulated KS statistics, indicating small p-values, and suggesting the existence of systematic errors, that we have not accounted for. Fig. 14 shows the CDF for the experimental covariance distributions of 5 step trajectories (dashed black lines), compared to the 40000-trajectory simulated distributions, using the mean covariances determined by pEMv2 (solid blue and cyan

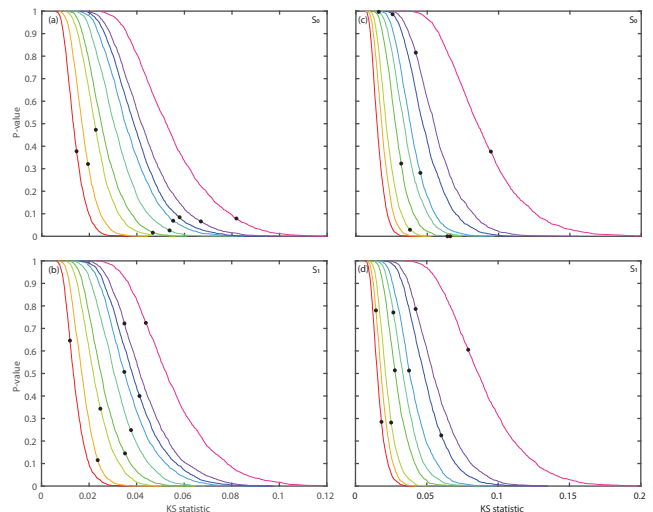


FIG. 12. p-values versus KS statistic for each track length, for TRAP-labeled Pma1 tracks, determined as described in the text by simulation, for state 1 [(a) and (b)] and state 2 [(c) and (d)], for S_0 and S_1 . Also shown is the analytic p-value according to the Kolmogorov distribution. The black circles correspond to the experimental KS statistics for each track length and their corresponding p-values. Track lengths shown: 5 (red), 6 (orange), 7 (light green), 8 (green), 9 (cyan), 10 (light blue), 11 (blue), 12 (purple), and 15 (magenta) steps.

lines). The simulated and experimental CDFs agree quite well, except for the S_0 distribution of state 2, where there is a noticeable experiment-theory discrepancy, that leads to the small p-value in this case.

Beyond $N = 6$ steps, the fourteen remaining S_0 p-values are larger than 0.01, and all but three of them are larger than 0.05. Fig. 15 and Fig. 16 show the CDFs for the experimental covariance distributions of 9 and 15 step trajectories, respectively (dashed black lines), compared to those of the simulated data set of 40000 tracks, using the mean covariances determined by pEMv2 (solid blue and cyan lines). For a track length of 9 steps, the simulated and experimental track CDFs agree quite well, although a small discrepancy between the CDFs of state 1 is apparent, which originates the smaller p-value in this case. For a track length of 15 steps, there are fewer experimental tracks, so the experimental CDFs unsurprisingly appear noisier than for shorter track lengths, but in this case the p-values are unremarkable. Overall, we consider that the collected p-values across all track lengths represents satisfactory agreement between the pEMv2-sorted distributions and theory and further supports pEMv2's finding that TRAP-labeled Pma1 exhibits 2 diffusive states, a mobile state with a diffusivity of about $0.16 \mu\text{m}^2\text{s}^{-1}$, and an essentially immobile state. It is not surprising that p-values are small when statistical noise is also small, and relatively large or unremarkable when the noise is larger, and can mask small, systematic errors.

Track Length	$p_{S_{01}}$	$p_{S_{02}}$	$KS_{S_{01}}$	$KS_{S_{02}}$	$p_{S_{11}}$	$p_{S_{12}}$	$KS_{S_{11}}$	$KS_{S_{12}}$	State 1 Tracks	State 2 Tracks
5	0.378	<0.0005	0.0146	0.0642	0.646	0.285	0.0120	0.0182	4406	3324
6	0.321	<0.0005	0.0194	0.0661	0.115	0.78	0.0236	0.0143	2486	2219
7	0.473	0.029	0.0227	0.0379	0.343	0.282	0.0247	0.0250	1432	1531
8	0.016	0.323	0.0467	0.0317	0.145	0.514	0.0352	0.0276	1067	895
9	0.026	0.997	0.0538	0.0160	0.249	0.771	0.0377	0.0266	746	628
10	0.069	0.281	0.0553	0.0452	0.507	0.513	0.0348	0.0375	547	474
11	0.0845	0.986	0.0580	0.0258	0.400	0.225	0.0412	0.0601	466	301
12	0.0660	0.816	0.0669	0.0420	0.722	0.787	0.0349	0.0421	387	226
15	0.0790	0.376	0.0819	0.0946	0.725	0.606	0.0438	0.0790	246	91

TABLE III. KS test results, comparing the experimental pEMv2-sorted TRAP-labeled Pma1 covariance distributions to 40000 simulated tracks based on pEMv2-found values. Shown are the p-values and KS statistics for the diagonal and one-off diagonal covariances for state 1 (S_{01} and S_{11} , respectively) and state 2 (S_{02} and S_{12} , respectively). p-values of <0.0005 correspond to experimental KS statistics outside of the range of simulated KS statistics.

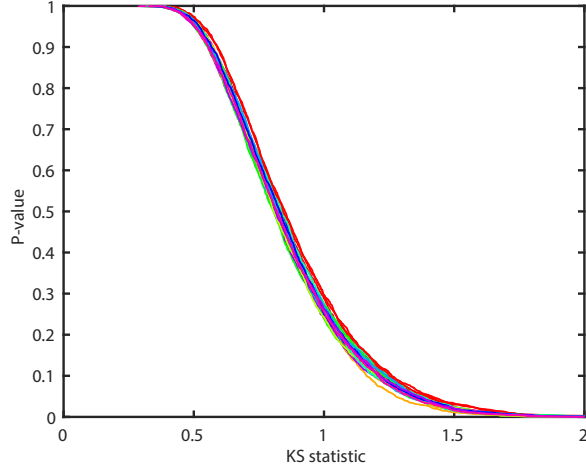


FIG. 13. p-values versus $\sqrt{\frac{n_1 n_2}{n_1 + n_2}} \times$ KS statistic, for TRAP-labeled Pma1 tracks, determined as described in the text by simulation, for state 1 and state 2, for S_0 and S_1 . Track lengths shown: 5 (red), 6 (orange), 7 (light green), 8 (green), 9 (cyan), 10 (light blue), 11 (blue), 12 (purple), and 15 (magenta) steps.

G. pEMv2 finds two states for simulations that mimic experiments on TRAP-labeled Pma1

As noted previously, pEMv2 is most reliable for large numbers of long tracks. To test self-consistency with the limited number of tracks available experimentally, that is, that pEMv2 is indeed able to correctly characterize a population of tracks with the diffusion and population parameters output from running pEMv2 on the experimental tracks, which are limited in length and number, we applied pEMv2 to a population of simulated tracks with parameters matching those found by pEMv2 for the experimental tracks. We chose $D_1 = 0.0047 \mu\text{m}^2 \text{s}^{-1}$, $\sigma_1^2 = 0.0027 \mu\text{m}^2$, $D_2 = 0.154 \mu\text{m}^2 \text{s}^{-1}$, $\sigma_2^2 = 0.0031 \mu\text{m}^2$, $\phi_1 = 0.545$, and $\phi_2 = 0.455$. For each track length, we applied pEMv2 to the same number of tracks as available experimentally. As illustrated in Fig. 17, for

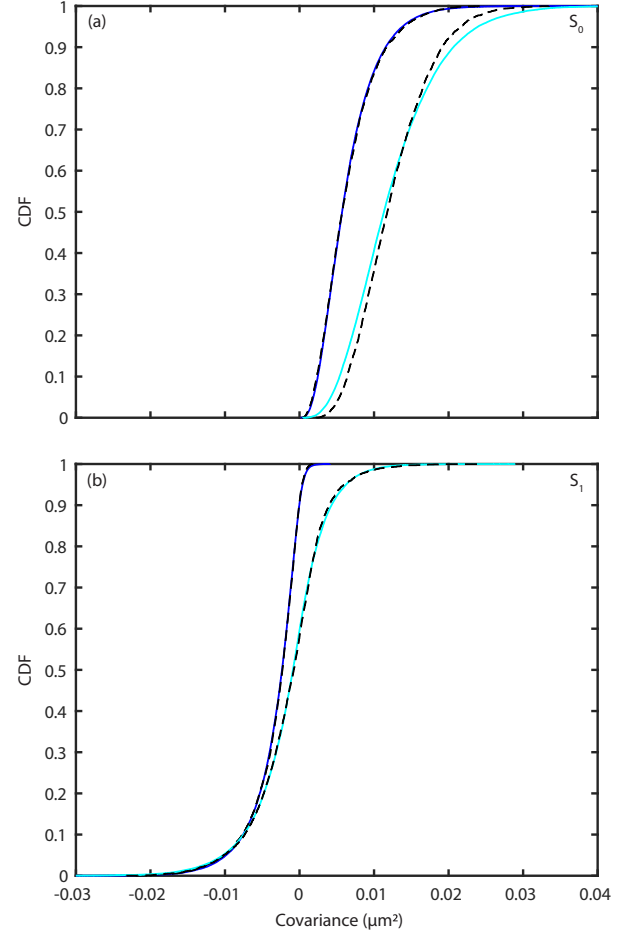


FIG. 14. Sorted CDFs for TRAP-labeled 5-step tracks. (a) pEMv2-sorted experimental S_0 distributions (black dashed lines) for state 1 and state 2, compared to 40000 simulated tracks for state 1 (blue) and state 2 (cyan). (b) pEMv2-sorted experimental S_1 distributions (black dashed lines) for state 1 and state 2, compared to 40000 simulated tracks for state 1 (blue) and state 2 (cyan).

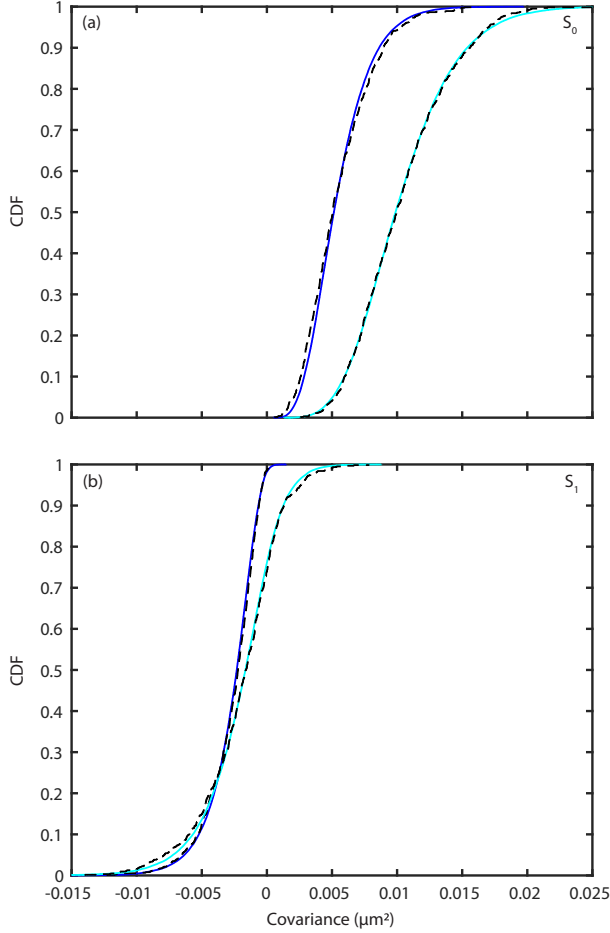


FIG. 15. Sorted CDFs for TRAP-labeled 9-step tracks. (a) pEMv2-sorted experimental S_0 distributions (black dashed lines) for state 1 and state 2, compared to 40000 simulated tracks for state 1 (blue) and state 2 (cyan). (b) pEMv2-sorted experimental S_1 distributions (black dashed lines) for state 1 and state 2, compared to 40000 simulated tracks for state 1 (blue) and state 2 (cyan).

each track length, pEMv2’s BIC showed a maximum for two diffusive states, consistent with what was simulated, *i.e.* consistent with the “ground truth”, and similar to the BICs for experimental trajectories (Fig. 6).

Fig. 18 depicts the simulated covariance distributions for a track length of 9 steps, together with the corresponding theoretical curves. The covariances sorted into their respective states, shown as the dark and darker grey histograms for states 1 and 2, respectively, agree well with the theoretical curves, shown as blue and cyan curves for states 1 and 2, respectively. Similarly, the unsorted simulated covariance distributions, shown as the light grey histograms, agree well with the two-component theory curves, shown as the red curves, and the best-fits, shown as the dashed black curves.

In Fig. 19, the covariance values determined by pEMv2 and by fitting are compared for different track lengths to

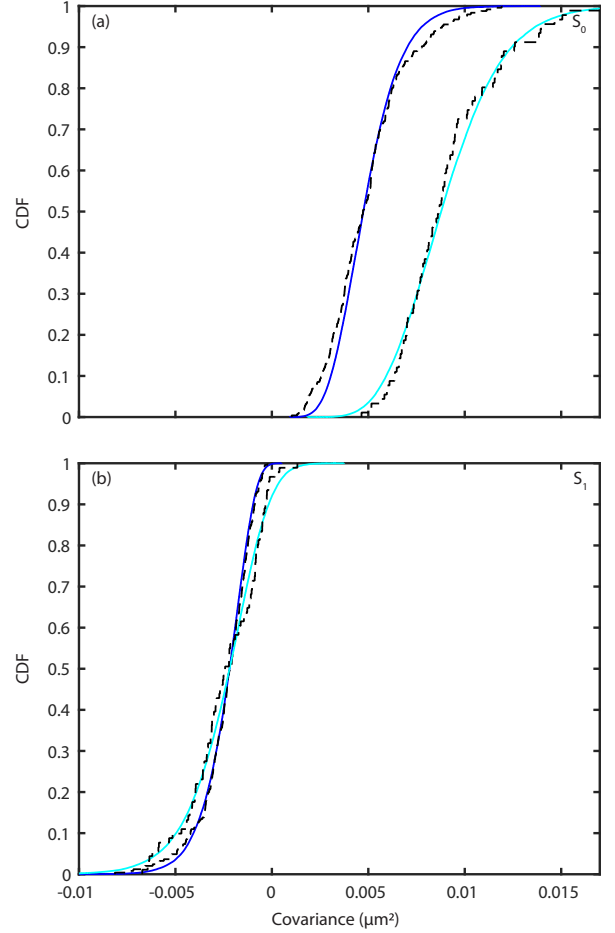


FIG. 16. Sorted CDFs for TRAP-labeled 15-step tracks. (a) pEMv2-sorted experimental S_0 distributions (black dashed lines) for state 1 and state 2, compared to 40000 simulated tracks for state 1 (blue) and state 2 (cyan). (b) pEMv2-sorted experimental S_1 distributions (black dashed lines) for state 1 and state 2, compared to 40000 simulated tracks for state 1 (blue) and state 2 (cyan).

the ground truth. For these simulated data, both fitted and pEMv2-sorted covariances appear constant and agree closely with the simulation parameters, across all track lengths. The distribution of diffusivities for 9-step simulated tracks also shows good agreement between theory (blue and cyan lines for this distribution sorted into two states, red lines for the unsorted distribution) and experimental distributions (Fig. 5(b)). In this case, $D_1 = 0.0030 \mu\text{m}^2 \text{s}^{-1}$, $\sigma_1^2 = 0.0028 \mu\text{m}^2$, and $D_2 = 0.169 \mu\text{m}^2 \text{s}^{-1}$, $\sigma_2^2 = 0.0029 \mu\text{m}^2$, very close to the ground truth values. Sorted simulated MSDs are displayed in Fig. 7(b), again showing the difference in diffusivity between the two sorted states, with the state 1 MSDs (blue) having much smaller slopes than the state 2 MSDs (cyan). In contrast to the MSDs for experimental TRAP-labeled Pma1 (Fig. 7(a)), the slopes of the state 2 MSDs do not vary significantly with increasing

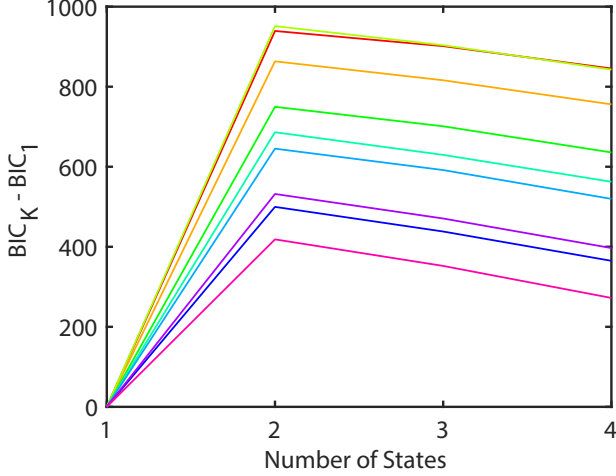


FIG. 17. Relative Bayesian Information Criterion ($BIC_K - BIC_1$) values versus number of diffusive states for simulated TRAP-labeled Pma1 trajectories of length 5 (red), 6 (orange), 7 (lime green), 8 (green), 9, (blue-green), 10 (blue), 11 (dark blue), 12 (purple), and 15 (magenta). The highest relative BIC value for each track length occurs for two states, irrespective of track length.

track length. This behavior is as expected, because the simulated tracks are constructed with the same diffusive parameters for all track lengths. From this analysis of simulated data, we may conclude that pEMv2 is well able to correctly identify and sort the experimental number of trajectories, possessing the pEMv2-determined diffusion parameters and population fractions.

H. pEMv2 finds two diffusive states for Pma1-mEos3.2 direct-fusion trajectories

Next, we applied pEMv2 and the theory of Sec. IID to Pma1-mEos3.2 direct-fusion trajectories. As shown in Fig. 20, for track lengths of 5, 6, 7, 8, 9, 10, 11, 12, and 15, the BIC was maximized for two states. However, the increase in the BIC, going from one state to two states, is much less in this case ($BIC_2 - BIC_1 = 250$), than for TRAP-labeled Pma1 trajectories ($BIC_2 - BIC_1 = 1000$, Fig. 6), indicating that pEMv2's preference for a two state description over a one-state description is much less for Pma1-mEos3.2 than for TRAP-labeled Pma1.

Table IV reports the mean covariances, \bar{S}_0 and \bar{S}_1 , the mean diffusivity, \bar{D} and the mean localization noise for the two diffusive states, found in this case, as well as the fraction of the population corresponding to state 1, ϕ_1 , the fraction of the population corresponding to state 2, ϕ_2 . From this table, it is clear that pEMv2 finds that Pma1-mEos3.2 is overall significantly less mobile than TRAP-labeled Pma1. First, the immobile state (state 1) constitutes about 90% of the total population. Second, the diffusivity of the higher diffusivity state (state

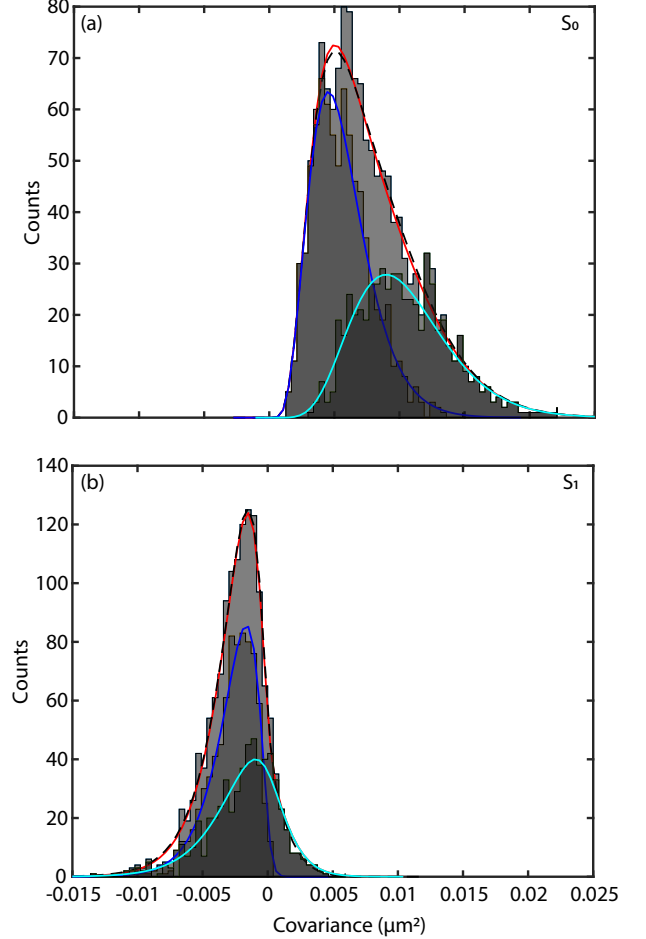


FIG. 18. Distribution of covariance elements, S_0 (a) and S_1 (b), for simulated TRAP-labeled Pma1 tracks of length 9 steps. The unsorted covariance distribution (light grey histogram) is plotted with the theoretical two-component curve (red curve) given by Eq. 11, and the fitted two-component curve (black dashed line). The tracks are sorted into two distributions representing the two distinct diffusive states found by pEMv2 (dark grey and darker grey histograms), and plotted with their single theory curves (blue and cyan curves), given by Eq. 4.

2) is just $D_2 \simeq 0.04 \mu\text{m}^2\text{s}^{-1}$, several times smaller than the diffusivity of TRAP-labeled Pma1's higher-diffusivity state, for which $D_2 \simeq 0.15 \mu\text{m}^2\text{s}^{-1}$. Hence, the more-mobile second state in this labeling method, is still far less mobile than the mobile state for the indirect labeling.

Fig. 22 shows the distribution of covariances for Pma1-mEos3.2 trajectories for a track length of 9 steps. The corresponding CDFs are shown in Fig. 29 and Fig. 31. For the direct fusion case too, we find good agreement between theory and experiment both for the sorted and unsorted distributions.

Fig. 21, Fig. 22, and Fig. 23 compare the experimental covariance distributions for Pma1-mEos3.2 trajectories with track lengths of 5, 9, and 15 steps, respectively, to

Track Length	\bar{S}_{01}	$\bar{S}_{01_{err}}$	\bar{S}_{11}	$\bar{S}_{02_{err}}$	D_1	$D_{1_{err}}$	σ_1^2	$\sigma_{1_{err}}^2$	\bar{S}_{02}	$\bar{S}_{02_{err}}$	\bar{S}_{12}	$\bar{S}_{12_{err}}$	D_2	$D_{2_{err}}$	σ_2^2	$\sigma_{2_{err}}^2$	ϕ_1	ϕ_2
5	0.0056	4.65×10^{-5}	-0.0029	4.19×10^{-5}	-0.0021	0.0013	0.0028	3.47×10^{-5}	0.0128	1.64×10^{-4}	-0.0048	1.78×10^{-4}	0.081	0.0063	0.0053	1.41×10^{-4}	0.84	0.16
6	0.0058	5.17×10^{-5}	-0.0029	4.27×10^{-5}	0.0012	0.0012	0.0029	3.61×10^{-5}	0.0123	2.00×10^{-4}	-0.0046	2.08×10^{-4}	0.079	0.0071	0.0051	1.673×10^{-4}	0.89	0.11
7	0.0053	5.03×10^{-5}	-0.0027	4.26×10^{-5}	0.00075	0.0013	0.0027	3.57×10^{-5}	0.0111	1.57×10^{-4}	-0.0047	1.56×10^{-4}	0.0448	0.0053	0.0050	1.26×10^{-4}	0.82	0.18
8	0.0057	5.76×10^{-5}	-0.0028	4.56×10^{-5}	0.0021	0.0013	0.0028	3.89×10^{-5}	0.0115	2.40×10^{-4}	-0.0045	2.32×10^{-4}	0.061	0.0075	0.0049	1.90×10^{-4}	0.91	0.09
9	0.0055	5.98×10^{-5}	-0.0027	4.72×10^{-5}	0.0015	0.0013	0.0027	4.03×10^{-5}	0.0107	2.14×10^{-4}	-0.0046	2.10×10^{-4}	0.040	0.0068	0.0048	1.70×10^{-4}	0.89	0.11
10	0.0054	6.18×10^{-5}	-0.0026	4.82×10^{-5}	0.0032	0.0014	0.0027	4.13×10^{-5}	0.0102	2.37×10^{-4}	-0.0044	2.16×10^{-4}	0.035	0.0066	0.0046	1.79×10^{-4}	0.89	0.11
11	0.0053	6.30×10^{-5}	-0.0026	4.81×10^{-5}	0.0020	0.0013	0.0026	4.14×10^{-5}	0.0100	2.32×10^{-4}	-0.0042	2.05×10^{-4}	0.032	0.0064	0.0044	1.70×10^{-4}	0.86	0.14
12	0.0049	5.90×10^{-5}	-0.0024	4.41×10^{-5}	0.0036	0.0013	0.0024	3.80×10^{-5}	0.0090	1.64×10^{-4}	-0.0042	1.45×10^{-4}	0.0136	0.0045	0.0043	1.20×10^{-4}	0.77	0.23
15	0.0050	6.80×10^{-5}	-0.0025	5.16×10^{-5}	0.0012	0.0014	0.0025	4.45×10^{-5}	0.0087	2.01×10^{-4}	-0.0040	1.80×10^{-4}	0.0166	0.00549	0.0041	1.50×10^{-4}	0.82	0.18

TABLE IV. Results from applying pEMv2 for direct fusion data: covariances (\bar{S}_0 and \bar{S}_1), diffusivities (D), localization errors (σ^2), and volume fractions (ϕ) for the two states found by pEMv2 for track lengths of $N = 5, 6, 7, 8, 9, 10, 11, 12$, and 15 .

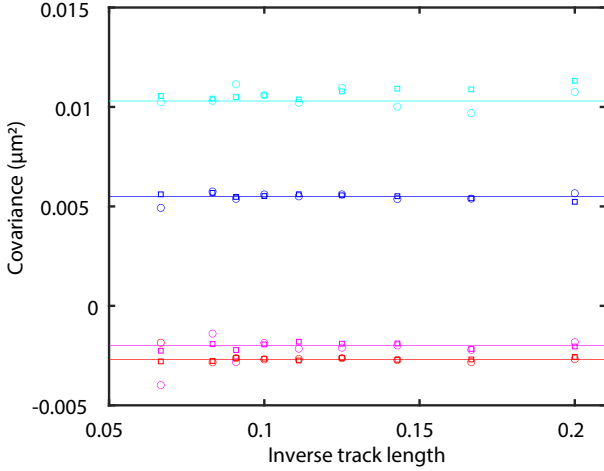


FIG. 19. Plot comparing the fitted S_0 and S_1 values (circles) to the pEMv2 found values (squares), versus inverse track length, for simulated TRAP-labeled Pma1. The S_0 values are in blue and cyan for states 1 and 2, respectively. The S_1 values are in red and magenta for states 1 and 2, respectively. Solid lines are the S values used in simulating the single particle trajectories, and are thus the 'ground truth' covariance element values.

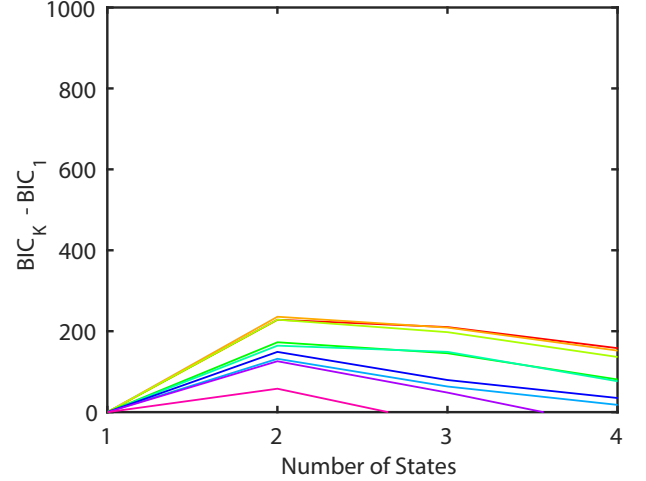


FIG. 20. Relative Bayesian Information Criterion ($BIC_K - BIC_1$) values versus number of diffusive states for Pma1-mEos3.2 direct fusion trajectories of length 5 (red), 6 (orange), 7 (lime green), 8 (green), 9 (blue-green), 10 (blue), 11 (dark blue), 12 (purple), and 15 (magenta). The highest relative BIC value for each track length occurs for two states, irrespective of track length.

the corresponding theoretical predictions. In each figure, there appears to be good agreement between theory and data, even though no fitting is involved. The fact that the distributions to emerge from the pEMv2-sorted populations agree well with what is expected theoretically supports that pEMv2 is correctly characterizing the diffusive behavior of Pma1-mEos3.2.

Fig. 5(c) shows the diffusivity distributions for Pma1-mEos3.2 trajectories. Two features stand out from this figure in comparison to Fig. 5(a). First, the population fraction of the higher diffusivity state (state 2) is significantly less for the direct fusion than for TRAP-labeled Pma1. Second, the mean diffusivity of the higher diffusivity state (state 2) is significantly less for the direct fusion ($\sim 0.05 \mu\text{m}^2\text{s}^{-1}$) than for TRAP-labeled Pma1 ($\sim 0.16 \mu\text{m}^2\text{s}^{-1}$). These two features make the overall diffusivity of Pma1-mEos3.2 significantly smaller than that of TRAP-labeled Pma1.

We also carried out a p-value analysis for Pma1-mEos3.2 tracks (presented in Table V, Fig. 24, and

Fig. 25), similar to our earlier p-value analysis for TRAP-labeled Pma1 tracks (Sec. IV F). For Pma1-mEos3.2, none of the eighteen p-values, associated with S_1 is less than 0.01. However, 7 of 18 p-values, associated with S_0 are less than 0.01, and 11 of 18 are less than 0.05. In this case too, the p-values are especially small for track lengths of $N = 5$ and $N = 6$ steps, as well as for track lengths of $N = 7$ and $N = 10$ steps. Overall, the p-values for Pma1-mEos3.2's S_0 seem smaller than for TRAP-labeled Pma1, indicating less overall agreement between experiment and theory in this case. Because the mobility of Pma1-mEos3.2 is smaller than for TRAP-labeled Pma1, we may expect that localization noise is a more dominant contributor to S_0 (and S_1) for Pma1-mEos3.2 than for TRAP-labeled Pma1. Therefore, because the theory assumes Gaussian localization noise, any deviation of the localization noise from Gaussian behavior may manifest as poorer experiment-theory agreement for Pma1-mEos3.2 than for TRAP-labeled Pma1. Previously, Ref. [18] showed that heterogeneity in the localiza-

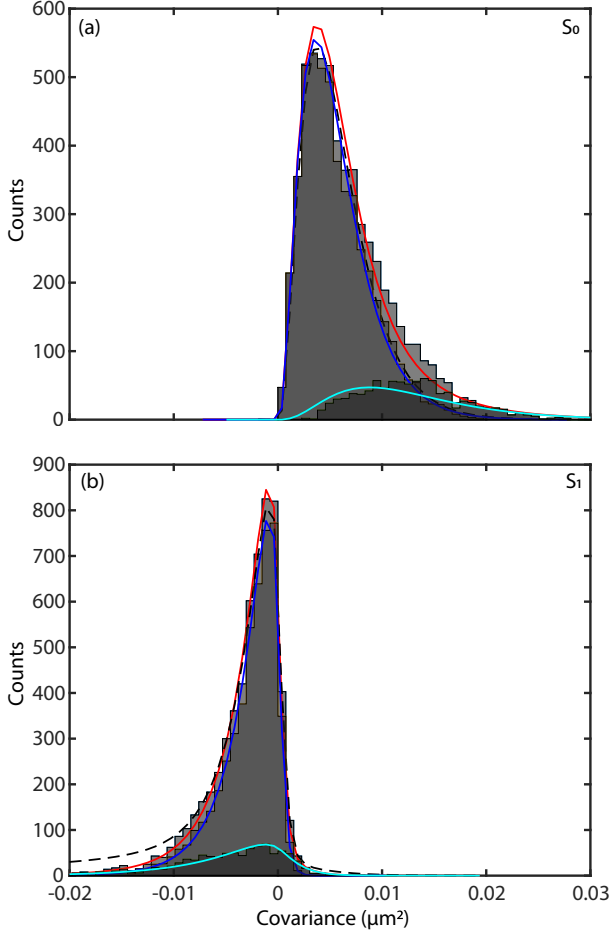


FIG. 21. Distribution of covariance elements, S_0 (a) and S_1 (b), for experimental direct fusion tracks of length 5 steps. The unsorted covariance distribution (light grey histogram) is plotted with the theoretical two-component curve (red curve) given by Eq. 11, and the fitted two-component curve (black dashed line). The tracks are sorted into two distributions representing the two distinct diffusive states found by pEMv2 (dark grey and darker grey histograms), and plotted with their single theory curves (blue and cyan curves), given by Eq. 4.

tion noise could account for discrepancies between experimental and predicted S_0 - and S_1 -distributions. However, in that case, the discrepancies became more important with increasing track length, which is not what we observe here.

V. CONCLUSION

Three important conclusions are to be drawn from this work. First, how a protein is labeled for microscopy visualization in living cells can affect its diffusive behavior in a substantial fashion with unknown consequences for its biological function. This observation emphasizes the

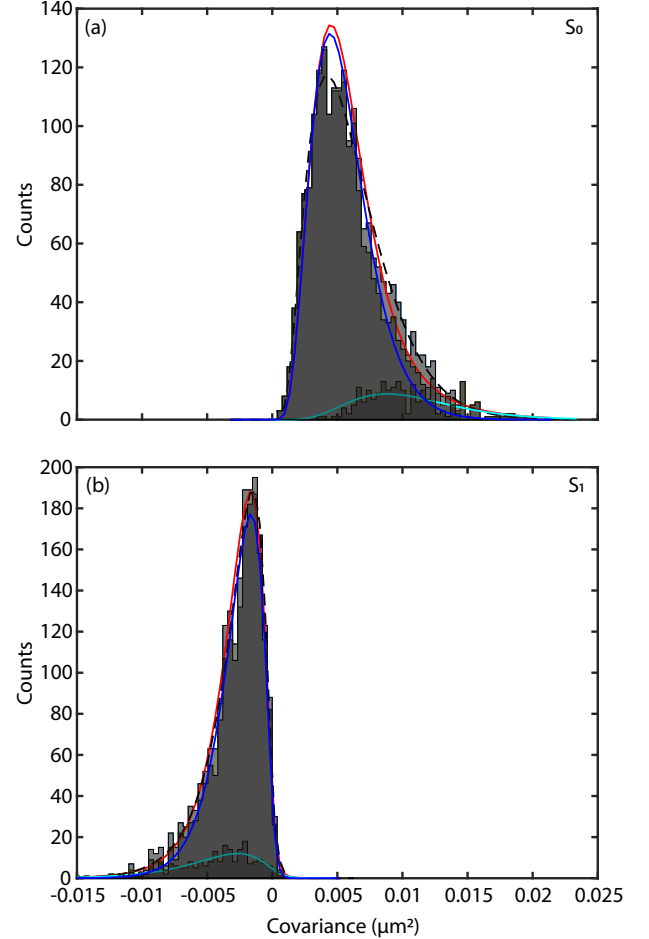


FIG. 22. Distribution of covariance elements, S_0 (a) and S_1 (b), for experimental direct fusion tracks of length 9 steps. The unsorted covariance distribution (light grey histogram) is plotted with the theoretical two-component curve (red curve) given by Eq. 11, and the fitted two-component curve (black dashed line). The tracks are sorted into two distributions representing the two distinct diffusive states found by pEMv2 (dark grey and darker grey histograms), and plotted with their single theory curves (blue and cyan curves), given by Eq. 4.

importance of the continuing development and enhancement of minimally-invasive labeling schemes for live cell studies [17]. Second, the diffusive behavior of Pma1 can be described convincingly in terms of two discrete diffusive states, each with its own diffusive properties. Third, both variants of Pma1 studied in this work, TRAP-labeled Pma1 and Pma1-mEos3.2, are monomers *in vivo*. Another result to emerge from this work is an estimate of the TRAP-peptide bound-state lifetime of 0.15 s. To be able to come to these conclusions, we investigated two differently labeled versions of Pma1 at the single molecule level using single particle tracking under TIRF illumination. Using a machine learning based approach that identifies and sorts a population of trajectories into a

Track Length	$p_{S_{01}}$	$p_{S_{02}}$	$KS_{S_{01}}$	$KS_{S_{02}}$	$p_{S_{11}}$	$p_{S_{12}}$	$KS_{S_{11}}$	$KS_{S_{12}}$	Tracks in State 1	Tracks in State 2
5	0.0085	<0.0005	0.0258	0.106	0.634	0.0695	0.0108	0.0426	4904	910
6	0.0360	<0.0005	0.0238	0.105	0.182	0.0784	0.0184	0.0561	3711	474
7	0.0280	<0.0005	0.0286	0.101	0.638	0.107	0.0151	0.0498	2634	577
8	0.001	0.0570	0.0392	0.0869	0.353	0.840	0.0197	0.0394	2301	239
9	0.00350	0.044	0.0426	0.0898	0.0805	753	0.0301	0.0441	1811	228
10	<0.0005	0.339	0.0601	0.0702	0.0770	0.9605	0.0341	0.0372	1493	179
11	0.0115	0.754	0.0482	0.0477	0.489	0.873	0.0242	0.0419	1212	192
12	0.486	0.221	0.0277	0.0626	0.787	0.474	0.0217	0.0510	922	274
15	0.0610	0.542	0.0514	0.0655	0.611	0.850	0.0297	0.0495	657	143

TABLE V. KS test results, comparing the experimental pEMv2-sorted direct fusion covariance distributions to 40000 simulated tracks based on pEMv2-found values. Shown are the p-values and KS statistics for the diagonal and one-off diagonal covariances for state 1 (S_{01} and S_{11} , respectively) and state 2 (S_{02} and S_{12} , respectively). p-values of <0.0005 correspond to experimental KS statistics outside of the range of simulated KS statistics.

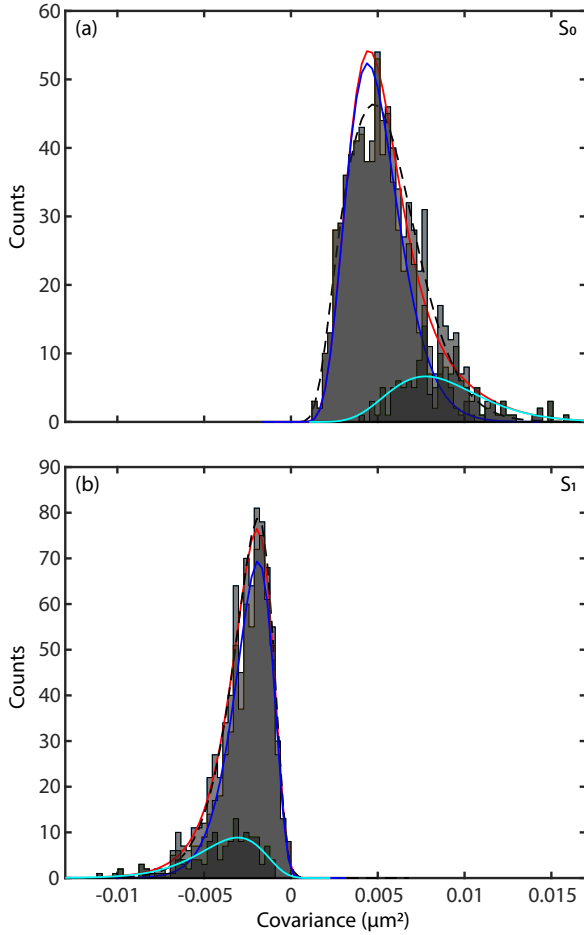


FIG. 23. Distribution of covariance elements, S_0 (a) and S_1 (b), for experimental direct fusion tracks of length 15 steps. The unsorted covariance distribution (light grey histogram) is plotted with the theoretical two-component curve (red curve) given by Eq. 11, and the fitted two-component curve (black dashed line). The tracks are sorted into two distributions representing the two distinct diffusive states found by pEMv2 (dark grey and darker grey histograms), and plotted with their single theory curves (blue and cyan curves), given by Eq. 4.

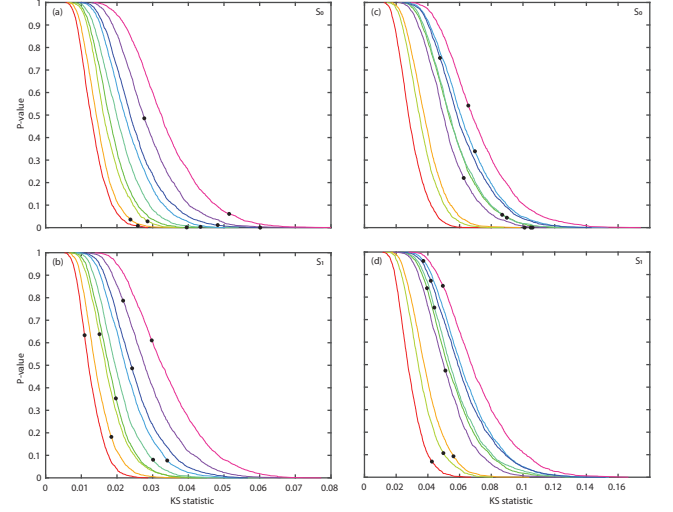


FIG. 24. p-values versus KS statistic for each track length, for direct fusion tracks, determined as described in the text by simulation, for state 1 (a and b) and state 2 (c and d), for S_0 and S_1 . Also shown is the analytic p-value according to the Kolmogorov distribution. The black circles correspond to the experimental KS statistics for each track length and their corresponding p-values. Track lengths shown: 5 (red), 6 (orange), 7 (light green), 8 (green), 9 (cyan), 10 (light blue), 11 (blue), 12 (purple), and 15 (magenta) steps.

discrete number of diffusive states, namely pEMv2, we found that a minimally-modified version of Pma1, with a C-terminal five-amino-acid tag that reversibly binds to a TRAP-mEos3.2 fusion, shows comparable population fractions of a mobile state, corresponding to simple diffusion with a diffusion constant consistent with what is expected for a membrane protein, and an essentially immobile state. By contrast, we found that a Pma1-mEos3.2 direct fusion is overwhelmingly in an immobile state, and the small population fraction, assigned to a more mobile state by pEMv2, has a diffusion coefficient several times smaller than the diffusion coefficient of mobile TRAP-labeled Pma1. A comparison between the experimental pEMv2-sorted covariance and diffusivity dis-

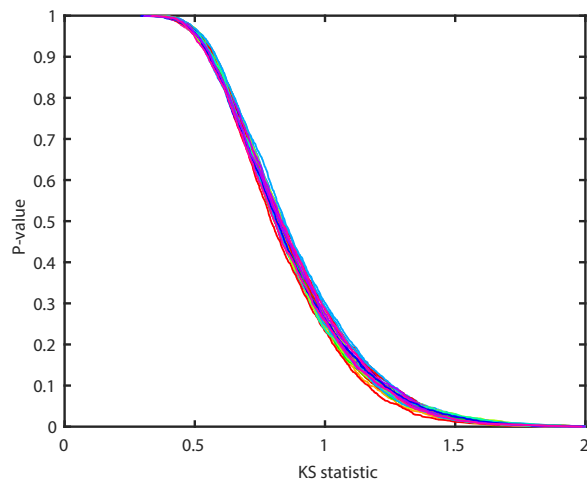


FIG. 25. p-values versus $\sqrt{\frac{n_1 n_2}{n_1 + n_2}} \times \text{KS statistic}$, for for direct fusion tracks, determined as described in the text by simulation, for state 1 and state 2, for S_0 and S_1 . Track lengths shown: 5 (red), 6 (orange), 7 (light green), 8 (green), 9 (cyan), 10 (light blue), 11 (blue), 12 (purple), and 15 (magenta) steps.

tributions, conditioned on the experimental mean covariances of the sorted tracks, and the corresponding theoret-

ical distributions shows overall good agreement without any fitting, providing strong support for pEMv2-based sorting. However, a detailed p-value analysis, based on the KS-statistic of experimental and simulated distributions, reveals the existence of (small) systematic errors, whose origin we do not yet understand. An open question remains as to whether Pmal1's two diffusive states are significant for Pmal1's biological function, and if so what their roles might be.

ACKNOWLEDGMENTS

M.L.P.B. and S.E.P. contributed equally to this work. M.L.P.B. conceived the project, analyzed data, and wrote the paper; S.E.P. conceived the project, collected data, analyzed data, and wrote the paper; Y.Z. conceived the project, collected data, and wrote the paper; M.H. conceived the project, constructed the yeast strains, and wrote the paper; J.B. conceived the project and wrote the paper; L.R. conceived the project and wrote the paper; S.G.J.M. conceived the project and wrote the paper. This research was supported by the National Institutes of Health via NIH R01 GM118528 and NIH P30 DK045735. M.L.P.B. was supported by NIH T32EB019941 and the NSF GRFP. S.E.P. was supported by the NSF GRFP and NSF PHYS 1522467.

-
- [1] R. W. Albers, *Biochemical aspects of active transport*, *Annual Review of Biochemistry* **36**, 727 (1967).
- [2] R. L. Post, C. Hegvary, and S. Kume, Activation by adenosine triphosphate in the phosphorylation kinetics of sodium and potassium ion transport adenosine triphosphatase, *Journal of Biological Chemistry* **247**, 6530 (1972).
- [3] E. Goormaghtigh, C. Chadwick, and G. A. Scarborough, Monomers of the neurospora plasma membrane H^+ -ATPase catalyze efficient proton translocation, *J. Biol. Chem.* **261**, 7466 (1986).
- [4] P. Morsomme, C. W. Slayman, and A. Goffeau, Mutagenic study of the structure, function and biogenesis of the yeast plasma membrane H^+ -atpase, *Biochimica et Biophysica Acta (BBA) - Reviews on Biomembranes* **1469**, 133 (2000).
- [5] K. Malinska, J. Malinsky, M. Opekarova, and W. Tanner, Visualization of protein compartmentation within the plasma membrane of living yeast cells, *Mol Biol Cell*, 4427 (2003).
- [6] W. Kühlbrandt, Biology, structure and mechanism of p-type ATPases, *Nature Reviews Molecular Cell Biology* **5**, 282 (2004).
- [7] F. Spira, N. S. Mueller, G. Beck, P. von Olshausen, J. Beig, and R. Wedlich-Soeldner, Patchwork organization of the yeast plasma membrane into numerous coexisting domains, *Nature Cell Biology* **14**, 640 (2012).
- [8] A. Mason and C. Slayman, P-type pumps: Plasma-membrane H^+ pumps, in *Encyclopedia of Biological Chemistry* (Elsevier, 2013) pp. 688–692.
- [9] K. A. Henderson, A. L. Hughes, and D. E. Gottschling, Mother-daughter asymmetry of pH underlies aging and rejuvenation in yeast, *eLife* **3**, 10.7554/elife.03504 (2014).
- [10] A. Athanasopoulos, B. Andre, V. Sophianopoulou, and C. Gournas, Fungal plasma membrane domains, *FEMS Microbiology Reviews* **43**, 642 (2019).
- [11] S. Heit, M. M. G. Geurts, B. J. Murphy, R. A. Corey, D. J. Mills, W. Kühlbrandt, and M. Bublitz, Structure of the hexameric fungal plasma membrane proton pump in its autoinhibited state, *Science Advances* **7**, eabj5255 (2021).
- [12] P. Zhao, C. Zhao, D. Chen, C. Yun, and L. Bai, Structure and activation mechanism of the hexameric plasma membrane H^+ -ATPase, *Nat. Commun.* **12**, 6439 (2021).
- [13] S. E. Pratt, E. B. Speltz, S. G. J. Mochrie, and L. Regan, Designed proteins as novel imaging reagents in LivingEscherichia coli, *ChemBioChem* **17**, 1652 (2016).
- [14] C. Oi, Z. Gidden, L. Holyoake, O. Kantelberg, S. Mochrie, M. H. Horrocks, and L. Regan, A step-by-step protocol for performing LIVE-PAINT super-resolution imaging of proteins in live cells using reversible peptide-protein interactions 10.21203/rs.3.pe-1043/v1 (2020).
- [15] M. Hinrichsen, M. Lenz, J. M. Edwards, O. K. Miller, S. G. J. Mochrie, P. S. Swain, U. Schwarz-Linek, and L. Regan, A new method for post-translationally labeling proteins in live cells for fluorescence imaging and tracking, *Protein Engineering, Design and Selection* **30**, 771

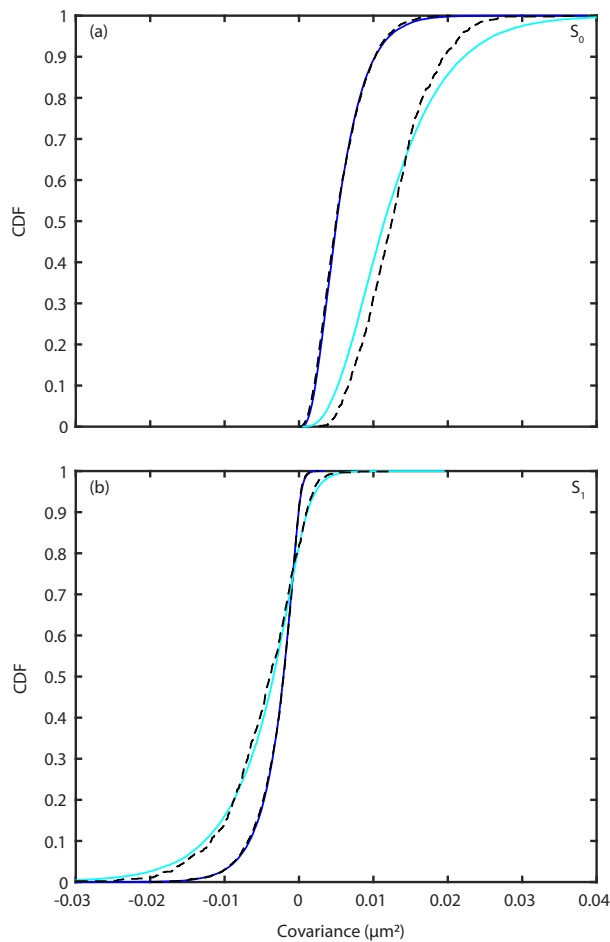


FIG. 26. Sorted CDFs of experimental direct fusion data for a track length of 5 steps. CDFs for (a) S_0 -distributions and (b) S_1 -distributions (black dashed lines) for each sorted state, compared to theory curves for each state (blue and cyan lines).

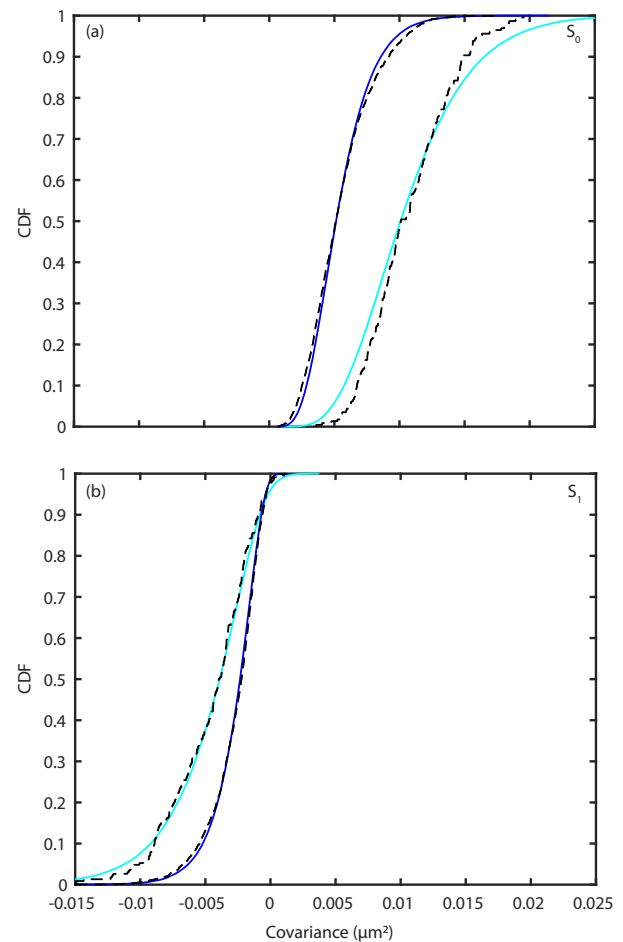


FIG. 27. Sorted CDFs of experimental direct fusion data for a track length of 9 steps. CDFs for (a) S_0 -distributions and (b) S_1 -distributions (black dashed lines) for each sorted state, compared to theory curves for each state (blue and cyan lines).

- (2017).
- [16] C. Oi, Z. Gidden, L. Holyoake, O. Kantelberg, S. Mochrie, M. H. Horrocks, and L. Regan, LIVE-PAINT allows super-resolution microscopy inside living cells using reversible peptide-protein interactions, *Communications Biology* **3**, 10.1038/s42003-020-01188-6 (2020).
- [17] C. Oi, S. G. J. Mochrie, M. H. Horrocks, and L. Regan, PAINT using proteins: A new brush for super-resolution artists, *Protein Science* **29**, 2142 (2020).
- [18] M. L. P. Bailey, H. Yan, I. Surovtsev, J. F. Williams, M. C. King, and S. G. J. Mochrie, Covariance distributions in single particle tracking, *Physical Review E* **103**, 10.1103/physreve.103.032405 (2021).
- [19] P. K. Koo, M. Weitzman, C. R. Sabanaygam, K. L. van Golen, and S. G. Mochrie, Extracting diffusive states of Rho GTPase in live cells: towards in vivo biochemistry, *PLoS Computational Biology* **11** (2015).
- [20] P. K. Koo and S. G. Mochrie, Systems-level approach to uncovering diffusive states and their transitions from single-particle trajectories, *Physical Review E* **94**, 052412 (2016).
- [21] I. Rey-Suarez, B. A. Wheatley, P. Koo, A. Bhanja, Z. Shu, S. Mochrie, W. Song, H. Shroff, and A. Upadhyaya, WASP family proteins regulate the mobility of the b cell receptor during signaling activation, *Nature Communications* **11**, 10.1038/s41467-020-14335-8 (2020).
- [22] C. L. Vestergaard, P. C. Blainey, and H. Flyvbjerg, Optimal estimation of diffusion coefficients from single-particle trajectories, *Physical Review E* **89**, 022726 (2014).
- [23] B. Justesen, R. Hansen, H. Martens, L. Theorin, M. Palmgren, K. Martinez, T. Pomorski, and A. Fuglsang, Active plasma membrane p-type H^+ -ATPase reconstituted into nanodiscs is a monomer, *J. Biol. Chem.* , 26419 (2013).
- [24] W.-K. Huh, J. V. Falvo, L. C. Gerke, A. S. Carroll, R. W. Howson, J. S. Weissman, and E. K. O'Shea, Global analysis of protein localization in budding yeast, *Nature* **425**, 686 (2003).

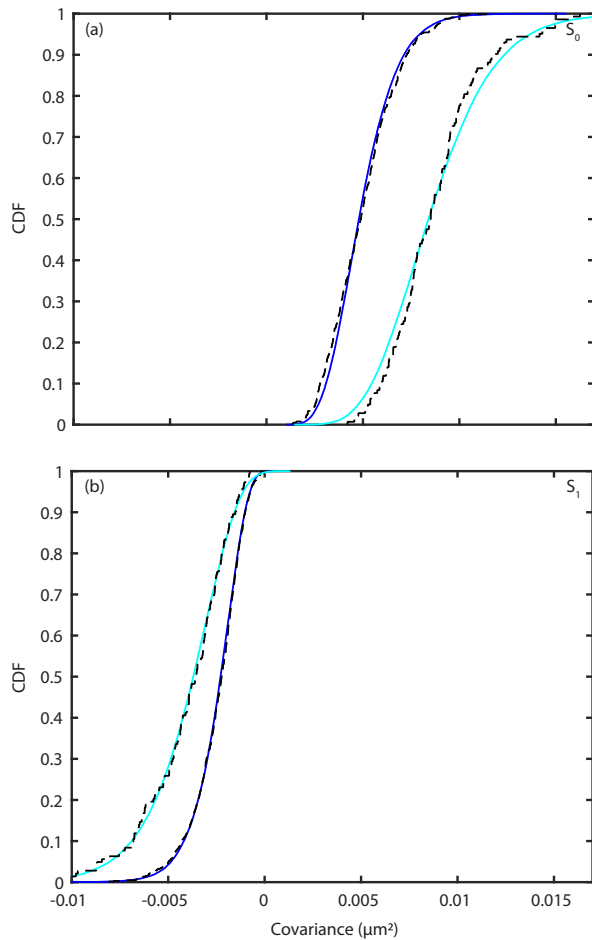


FIG. 28. Sorted CDFs of experimental direct fusion data for a track length of 15 steps. CDFs for (a) S_0 -distributions and (b) S_1 -distributions (black dashed lines) for each sorted state, compared to theory curves for each state (blue and cyan lines).

- [25] D. L. Coutu and T. Schroeder, Probing cellular processes by long-term live imaging – historic problems and current solutions, *Journal of Cell Science* 10.1242/jcs.118349 (2013).
- [26] C. Li, A. Tebo, and A. Gautier, Fluorogenic labeling strategies for biological imaging, *International Journal of Molecular Sciences* **18**, 1473 (2017).
- [27] C. P. Toseland, Fluorescent labeling and modification of proteins, *Journal of Chemical Biology* **6**, 85 (2013).
- [28] E. C. Jensen, Use of fluorescent probes: Their effect on cell biology and limitations, *The Anatomical Record: Advances in Integrative Anatomy and Evolutionary Biology* **295**, 2031 (2012).
- [29] M. Saxton, Single-particle tracking: the distribution of diffusion coefficients, *Biophysical Journal* **72**, 1744 (1997).
- [30] T. Savin and P. S. Doyle, Statistical and sampling issues when using multiple particle tracking, *Physical Review E* **76**, 10.1103/physreve.76.021501 (2007).

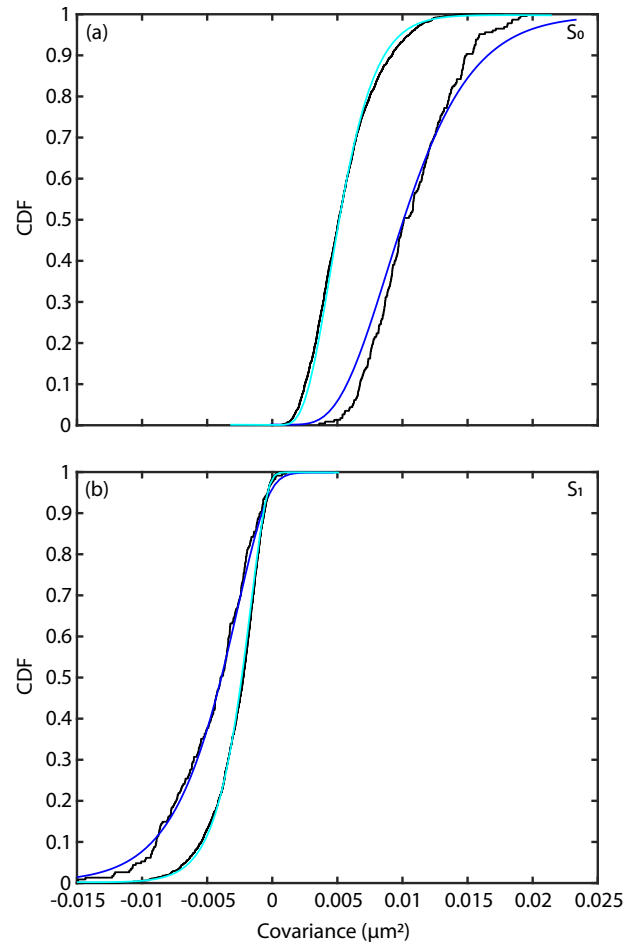


FIG. 29. Sorted CDFs of experimental direct fusion data for a track length of 9 steps. CDFs for sorted (a) S_0 -distributions and (b) S_1 -distributions (black lines) for each sorted state, compared to theory curves for each state (blue and cyan lines).

- [31] N. Monnier, Z. Barry, H. Y. Park, K.-C. Su, Z. Katz, B. P. English, A. Dey, K. Pan, I. M. Cheeseman, R. H. Singer, and M. Bathe, Inferring transient particle transport dynamics in live cells, *Nature Methods* **12**, 838 (2015).
- [32] R. Das, C. W. Cairo, and D. Coombs, A hidden markov model for single particle tracks quantifies dynamic interactions between LFA-1 and the actin cytoskeleton, *PLoS Computational Biology* **5**, e1000556 (2009).
- [33] P. J. Slator, C. W. Cairo, and N. J. Burroughs, Detection of diffusion heterogeneity in single particle tracking trajectories using a hidden markov model with measurement noise propagation, *PLOS ONE* **10**, e0140759 (2015).
- [34] R. Zhao, J. Yuan, N. Li, Y. Sun, T. Xia, and X. Fang, Analysis of the diffusivity change from single-molecule trajectories on living cells, *Analytical Chemistry* **91**, 13390 (2019).
- [35] H. D. Pinholt, S. S.-R. Bohr, J. F. Iversen, W. Boomsma, and N. S. Hatzakis, Single-particle diffusional fingerprinting: A machine-learning framework for quantitative analysis of heterogeneous diffusion, *Proceedings of the Na-*

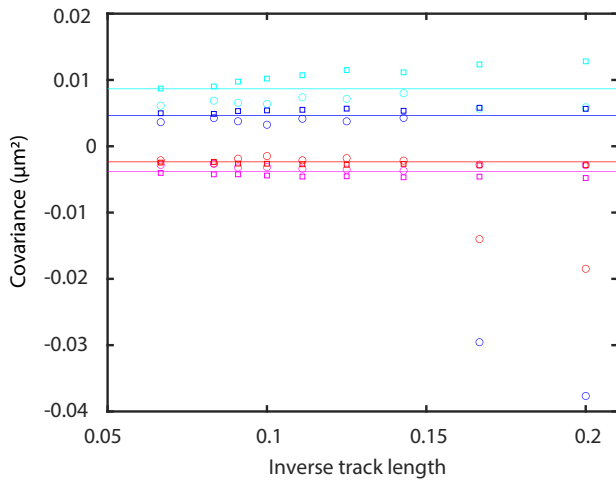


FIG. 30. Plot comparing the fitted S_0 and S_1 values (circles) to the pEMv2 found values (squares), versus inverse track length, for experimental direct fusion data. The S_0 values are in blue and cyan for states 1 and 2, respectively. The S_1 values are in red and magenta for states 1 and 2, respectively. Solid lines represent guides to the data, and are calculated by taking the average of the S values for each state over the track lengths.

- tional Academy of Sciences **118**, e2104624118 (2021).
- [36] M. Hinrichsen, *Applying protein-peptide interactions to fluorescently label proteins in *S. Cerevisiae**, Ph.D. thesis, Yale University (2018).
- [37] Y. Zhang, M. Lara-Tejero, J. Bewersdorf, and J. E. Galán, Visualization and characterization of individual type III protein secretion machines in live bacteria, *Proceedings of the National Academy of Sciences* **114**, 6098 (2017).
- [38] J. C. Crocker and D. G. Grier, Methods of digital video microscopy for colloidal studies, *Journal of Colloid and Interface Science* **179**, 298 (1996).
- [39] C. Oi, *Reversible Peptide-Protein Interactions Inside Cells: Enabling a New Approach for Achieving Super-Resolution Imaging in Live Cells*, Ph.D. thesis, Yale University (2021).
- [40] M. Kumar, M. S. Mommer, and V. Sourjik, Mobility of cytoplasmic, membrane, and DNA-binding proteins in *Escherichia coli*, *Biophysical Journal* **98**, 552 (2010).

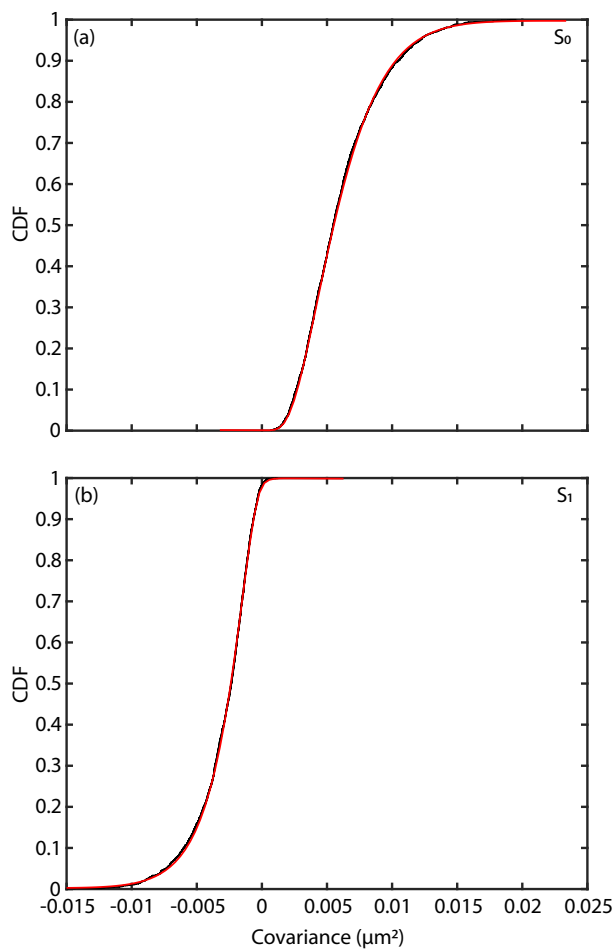


FIG. 31. CDFs of experimental direct fusion data for a track length of 9 steps. Comparison of CDFs for unsorted S_0 (a) and S_1 (b) distributions (black lines) to fitted theory curves (red lines).